Check for updates

International Journal of Energy Research

WILEY

RESEARCH ARTICLE OPEN ACCESS

Robust State of Charge Estimation of a Lithium Iron Phosphate Battery Module Using a Dual-UKF Under Various Operational Temperatures

Jun-Hyeong Kim[1] | Eunji Kwak[1] | Jinho Jeong[1] | Ki-Yong Oh[1,2]

[1]Department of Mechanical Convergence Engineering, Hanyang University, 222 Wangsimni-ro, Seongdong-gu, Seoul 04763, Republic of Korea | [2]School of Mechanical Engineering, Hanyang University, 222 Wangsimni-ro, Seongdong-gu, Seoul 04763, Republic of Korea

Correspondence: Ki-Yong Oh (kiyongoh@hanyang.ac.kr)

Received: 1 February 2026 | **Revised:** 26 August 2026 | **Accepted:** 8 September 2026

Keywords: energy storage system | lithium iron phosphate | lithium-ion battery | open circuit potential | state of charge

ABSTRACT

This paper proposes a robust framework to estimate the state of charge (SOC) of a lithium iron phosphate (LFP) battery module operating under diverse temperature conditions. The proposed framework integrates an enhanced equivalent circuit model (EECM) with a dual unscented Kalman filter (dual-UKF) to address SOC inconsistency and temperature-dependent nonlinearity in LFP modules. Bayesian optimization (BO) is employed to identify both model parameters and filter hyperparameters systematically, ensuring high fidelity and adaptability without manual tuning. The dual-loop UKF architecture simultaneously estimates SOC and updates time-varying parameters, effectively compensating for initialization errors of up to 10%. The proposed framework maintains an SOC root-mean-square error (RMSE) below 1% across a wide temperature range from −15 to 45°C, with a faster convergence observed at low temperatures caused by enhanced observability from increased potential variations. Comprehensive experimental validation using standard dynamic driving cycles and real-world stochastic battery energy storage system (BESS) data confirms the accuracy, robustness, and applicability of the proposed framework. Thus, the proposed framework offers a practical solution for battery management systems (BMSs) in LFP-based battery applications, as it provides accurate monitoring capabilities under diverse environmental and operational uncertainties.

1 | Introduction

Lithium iron phosphate (LFP) batteries are widely employed as the dominant power source in applications ranging from electric vehicles (EVs) to large-scale battery energy storage systems (BESSs) because of their superior thermal stability, long cycle life, and cost-effectiveness compared with that of nickel-based lithium-ion batteries (LIBs) [1–3]. However, the accurate state estimation for LFP batteries has recently emerged as a critical challenge, as the LFP chemistry exhibits an extremely flat open-circuit voltage (OCV) plateau and significant potential hysteresis [4, 5]. The weak observability of the state of charge (SOC) from the terminal potential of LFP batteries increases the risk of inaccurate estimation, resulting in inefficient energy utilization and potential thermal runaway caused by unintended overcharging or over-discharging [6, 7]. In addition, actual battery systems operate under diverse conditions and temperature variations [8]. A robust SOC estimation strategy is essential for deployment within a battery management system (BMS) [9, 10]. Hence, a robust estimation framework is indispensable when considering temperature-dependent nonlinearities and systemic uncertainties.

The Coulomb counting method was utilized as the foundation for SOC estimation in early BMS applications because of its low computational complexity as an open-loop method [11].

This is an open access article under the terms of the Creative Commons Attribution License, which permits use, distribution and reproduction in any medium, provided the original work is properly cited.

Copyright © 2026 Jun-Hyeong Kim et al. *International Journal of Energy Research* published by John Wiley & Sons Ltd.

This method calculated the remaining capacity by integrating the current flowing through the LIB over time. However, the accumulation of sensor measurement errors and lack of a feedback mechanism considerably limited the application of this method [12]. The initial SOC should be accurately identified because the estimation error persists and propagates throughout the operation owing to the lack of a feedback mechanism [13]. Consequently, a calibration mechanism based on the correlation between the terminal potential and SOC is required to mitigate concerns regarding these accumulated errors and correct the initial offset. OCV methods conventionally recalibrate the SOC using a lookup table of the thermodynamic relationship between the relaxation potential and its corresponding SOC [14]. However, the OCV method is impractical for real-time applications because obtaining a true OCV requires a long rest period for depolarizing Li ions, interrupting continuous operation [15]. Further, applying the OCV method to LFP cells is challenging because of their unique electrochemical characteristics [16]. The LFP chemistry exhibits an extremely flat OCV plateau across a wide SOC range (typically 10%–90%) [17], and even a minor potential measurement error can induce a significant SOC estimation error.

Thus far, several high-fidelity physics-based models have been proposed to address the complexities of internal battery states by overcoming limitations inherent in the OCV method. The pseudo-two-dimensional model based on porous electrode theory is a representative approach that describes the dynamics of lithium-ion concentration, potential distribution, and intercalation kinetics by addressing coupled partial differential equations (PDEs) [18, 19]. Enhanced single-particle models have been developed to characterize diffusion dynamics and thermal behavior with reduced complexity [20]. However, physics-based models suffer from excessive computational burden because solving coupled PDEs requires significant computational power, which suggests that these approaches are impractical for real-time onboard applications [21]. This limitation indicates that a computationally efficient model is essential for real-time control in the onboard applications of the BMS. Thus, equivalent circuit models (ECMs) are required for LFP batteries [22].

Several control-oriented models utilizing ECMs have been proposed [22–24]. Thevenin models were developed by integrating an ideal potential source with R-C networks for achieving a low computational cost [25]. Second-order R-C models have been introduced for investigating polarization characteristics and reducing modeling errors in dynamic profiles [26]. In addition, an adaptive ECM was developed for SOC estimation by employing the forgetting factor recursive least squares method and Kalman filter [27]. These models estimate the SOC at the single-cell level, which is suitable for BMS. However, these single-cell-based models have limitations in providing accurate estimations of LFP modules, as they fail to consider cell-to-cell inconsistencies [28]. The LFP module includes multiple cells connected in series and parallel (e.g., 2s4p), suggesting that module-level electrochemical dynamics play a critical role in improving the capability of BMSs. Thus, an ECM that considers SOC inconsistency is indispensable when considering module-level SOC inconsistency.

Several studies have focused on enhancing the robustness of SOC estimation algorithms. One study proposed a framework that integrated an electrochemical model and an extended Kalman filter (EKF) to estimate internal states [29]. An unscented Kalman filter (UKF) is a type of sigma-point Kalman filter that utilizes the unscented transform (UT) to estimate the SOC of LIBs in real time by effectively handling nonlinearities that limit the EKF [30]. The UKF outperformed the EKF by employing a UT sampling approach to approximate probability distribution, avoiding linearization errors associated with Jacobians used in the EKF [31]. These algorithms can accurately estimate the SOC by employing a nonlinear state observer. However, the performance of these model-based methods depends on the accurate identification of model parameters and tuning of filter hyperparameters [32]. In addition, manual tuning through trial and error is not only time-consuming but also fails to guarantee optimal performance under varying conditions [33]. Therefore, a systematic optimization method for parameter identification is essential for an SOC estimation framework.

Various studies have investigated parameter identification to identify optimal parameters for accurate SOC estimation. Comprehensive experiments revealed that parameters of ECMs vary significantly with temperature, and these variations affect the accuracy of the SOC estimation [34, 35]. Moreover, research showed that the noise characteristics of sensors vary based on the operating environment, which implies that the robustness of the UKF is strictly determined by hyperparameter initialization [36]. Hence, a framework that can systematically identify the optimal model parameters and filter-related hyperparameters is indispensable when enhancing the BMS performance under wide temperature ranges and stochastic load conditions.

To overcome these limitations, this study proposes a robust SOC estimation framework that integrates an enhanced ECM (EECM) and a dual-UKF optimized via Bayesian optimization (BO). To the best of our knowledge, the proposed framework is the first approach that can accurately estimate both SOC and potential in real-world stochastic BESS operations in real time. The novelty and key contributions of the proposed framework are listed below.

1. This paper proposes an EECM specifically designed to capture the nonlinear electrochemical characteristics of an LFP module by incorporating combined hysteresis effects and considering module-level SOC inconsistencies in a 2s4p configuration. The proposed model effectively mitigates observability limitations caused by the flat OCV plateau of the LFP chemistry.
2. A systematic optimization framework is established using BO to eliminate heuristic trial-and-error processes associated with parameter tuning. This approach simultaneously optimizes the physical parameters of the EECM and stochastic hyperparameters of the dual-UKF. This optimization ensures the robustness of the framework against sensor noise and environmental uncertainties.
3. The dual-UKF architecture is implemented to estimate the SOC and terminal potential in real time. This dual-loop structure recursively updates the time-varying model parameters to adapt to temperature-dependent nonlinear dynamics. Consequently, the proposed architecture ensures rapid convergence and high estimation accuracy even under severe initialization errors and dynamic load variations.

ijer, 2026, 1, Downloaded from https://onlinelibrary.wiley.com/doi/10.1155/er/7965949 by Hanyang University Library, Wiley Online Library on [01/11/2026]. See the Terms and Conditions (https://onlinelibrary.wiley.com/terms-and-conditions) on Wiley Online Library for rules of use; OA articles are governed by the applicable Creative Commons License

4. Comprehensive experiments are conducted, and the results confirm that the proposed framework accurately estimates the SOC and potential under various dynamic driving cycles across a wide temperature range as well as under real-world stochastic protocols from a residential BESS. The proposed framework demonstrates superior robustness against temperature-dependent nonlinearities, ensuring the reliability of the SOC estimation for actual field-deployed systems.

The remainder of this paper is organized as follows: Section 2 presents the experimental setup. Section 3 presents the integrated modeling and estimation framework, including the development of the EECM, formulation of the dual-UKF, and application of BO. Section 4 presents and discusses validation results under various static, dynamic, and real-world operating conditions; the applicability of the proposed method to real-world BESS protocols is also discussed. Finally, Section 5 presents the conclusions of this study and recommendations for future research.

2 | Experimental

The electrochemical and thermal characteristics of the LFP cell and module were examined to construct the proposed SOC estimation method using a test bed (Figure 1a). The testbed enables the precise measurement of potential, current, and temperature, which are essential for characterizing the electrical and thermal responses of LIBs. Battery test equipment (MACCOR Series 4000, USA) was employed to precisely control the charging and discharging operations under various test protocols. The terminal potential, current, and accumulated capacity were recorded at a sampling interval of 1 s using the test equipment during the experiments. The LIBs were placed in an environmental chamber (Jeiotech LCH-11-2C, South Korea) to control the ambient temperature in the test bed for electrochemical–thermal characterization (Figure 1a). A T-type thermocouple with an accuracy of ±1°C was installed at the surface center because temperature directly affects the electrochemistry of LIBs [37]. Note that the measured potential, current, temperature, and accumulated capacity were recorded at a sampling interval of 1 s during the laboratory experiments. Therefore, the dual-UKF was updated every 1 s for the dynamic stress test (DST), federal urban driving schedule (FUDS), and US06 driving cycle evaluations. In contrast, the field-monitoring data for the BESS operating conditions were recorded at 1 min intervals to facilitate efficient construction and management of the long-term operational database. The original 1 min time resolution was retained during the BESS validation, and the SOC estimate was updated whenever a new measurement record became available.

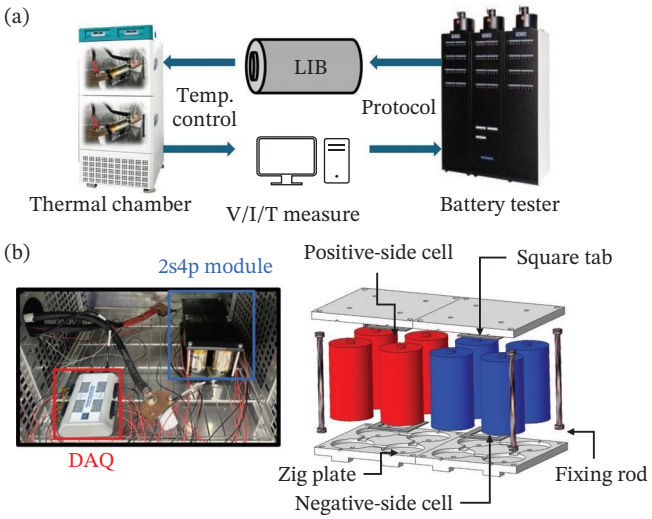

FIGURE 1 | (a) Experimental testbeds for a lithium-ion battery. (b) Positions of the LFP module inside the thermal chamber and the 2s4p configuration of the LFP module.

The specifications of the LFP cell and module used in the experiments are listed in Table 1. Experiments were performed with the LFP cell to not only estimate the parameters addressed in the EECM but also validate the accuracy and robustness of the proposed method. ECCM was addressed in the LFP module. The LFP module is examined (Figure 1b) to clarify the SOC imbalance characteristics in the LIB module [38]. The SOC of each cell inside the module was not identical because of differences in the internal resistance of the cells, variations in cell capacity, and tab resistance effects of the fixtures [39]. This SOC nonuniformity was defined as SOC inconsistency, which resulted in nonuniform internal temperatures within the cell. Thus, cumulative SOC inconsistency caused adverse effects, including overcharging or overdischarging in certain cells [39]. These phenomena confirmed that the SOC inconsistency of the LFP module could be considered as the SOC inconsistency played a critical role in SOC estimation and modeling.

The LFP module comprises four LFP cells connected in parallel on each side; these two parallel groups are connected in series to form a 2s4p configuration (Figure 1b). Among the 4680 LFP cells, eight cells were connected to the LFP module using an aluminum square-type tab for minimizing temperature nonuniformity among the cells [40]. The square tab uniformly distributed the current to the parallel cells on each side. The distance between the centers of the LFP cells was set to 100 mm to maintain a uniform temperature within the LFP module. This configuration was appropriated for maintaining a consistent temperature distribution in the LFP module as the thermal chamber operates with an air-cooling flow.

This study employed three protocols to characterize the electrochemical and thermal properties of the LFP module. The first experiment characterized the OCV to estimate the pseudo-OCV;

TABLE 1 | Geometric and material parameters of the LFP cell and LFP module.

Properties	LFP cell	LFP module
Radius (mm)	46	46 for each cell
Height (mm)	80	80 for each cell
Charge cut-off potential (V)	2.0	4.0
Discharge cut-off potential(V)	3.6	7.2
Capacity (Ah)	15	60
Nominal potential (V)	3.2	6.4
Nominal energy (Wh)	48	384

ijer, 2026, 1, Downloaded from https://onlinelibrary.wiley.com/doi/10.1155/er/7965949 by Hanyang University Library, Wiley Online Library on [01/11/2026]. See the Terms and Conditions (https://onlinelibrary.wiley.com/terms-and-conditions) on Wiley Online Library for rules of use; OA articles are governed by the applicable Creative Commons License

the second experiment validated the proposed method for SOC estimation based on a standardized cycle under dynamic conditions; and the third experiment validated the BESS protocol, ensuring that the proposed method maintained a high estimation accuracy even in the presence of environmental disturbances.

The LFP and 2s4p LFP modules were charged and discharged at a rate of 1/30 C to measure the OCV (Figure 2a). This was essential for accurately characterizing the electrochemical–thermal behavior of the proposed method [41]. The LIB cell and module were charged at a constant current rate of C/30 until the upper cut-off potential was reached, followed by a 2 h rest period at a fixed temperature to ensure thermal equilibrium. Subsequently, the cell was discharged at a constant current rate of C/30 to the lower cut-off potential and rested for 2 h under the same temperature conditions. Table 1 indicates that the charge and discharge cut-off potentials are 3.6 and 2.0 V for the LFP cell of interest, respectively, whereas those for the LFP module are 7.2 and 4.0 V, respectively. These experiments were repeated at different environmental temperatures of −15, −5, 5, 15, 25, 35, and 45°C to consider temperature dependency on the OCV of the LIB cell and module. These datasets were used to estimate the pseudo-OCV look-up table as a function of the SOC (Figure 2b). The detailed pseudo-OCV estimation method is explained in Appendix A. The OCV-constructed dependence of temperature enables the proposed method to consider the temperature effect of diffusivity and reactivity on electrochemical–thermal responses, compensating for the temperature-dependent OCV hysteresis [42].

Three representative protocols were deployed in the LIB module. The DST protocol employs a stepwise dynamic current profile designed to evaluate the battery response under varying load conditions [43]. The highway driving schedule (US06) protocol simulates aggressive highway driving behavior characterized by rapid current transients [44]. The FUDS reflects an urban driving environment that comprises frequent acceleration and deceleration segments derived from standardized automotive test profiles [45]. The US06 and FUDS profiles exhibited significantly higher current fluctuations than the DST, indicating the robustness of the proposed method. In these experiments, dynamic current profiles were imposed under various temperature conditions across a wide range from −15 to 45°C in increments of 10°C for analyzing the effect on the temperature for the dynamic cycling characteristics of the LFP cell and module. Each cell and module was charged using a 1C constant-current constant-potential profile until the corresponding charge cut-off potential was reached. The DST, US06, and FUDS cycles were subsequently applied repeatedly without rest periods. The durations of one complete cycle for FUDS, US06, and DST were 1372, 600, and 916 s, respectively. Each cycle resulted in a partial discharge of the LIBs, resulting in a progressive decrease in the SOC with repeated cycling. Therefore, dynamic profiles were executed continuously until the discharge cutoff potential was reached to ensure full coverage of the SOC range from 100% to 0%. Hence, current, potential, and SOC trajectories obtained from these dynamic load experiments are used as benchmark datasets to validate the SOC estimation performance across the entire range of operating temperatures.

Real-world operational data collected from residential BESS in Northern Europe were employed for further validating the robustness and applicability of the proposed method for SOC estimation. The experimental protocol, including the current and temperature, was generated based on 1 month of monitoring data collected from a residential BESS operating under real-world conditions. Figure 3a–c shows that BESS data comprise monthly potential, current, and temperature measurements recorded under naturally varying conditions. Real-world BESS protocols inherently capture fluctuations in temperature, load demand, and user-dependent stochastic behavior [46]. Conventional laboratory experiments are examined at a fixed predefined temperature, which implies that the BESS protocol offers a more realistic representation of dynamic electrothermal characteristics [47]. The BESS protocol was collected during March, August, and December to account for seasonal and thermal variabilities. This seasonal sampling strategy enables the characterization of temperature-dependent stochastic current patterns, which differ significantly between high- and low-temperature months because of variations in household load usage. Hence, the proposed method for SOC estimation is validated using this dataset to determine if its performance extends beyond laboratory-controlled scenarios.

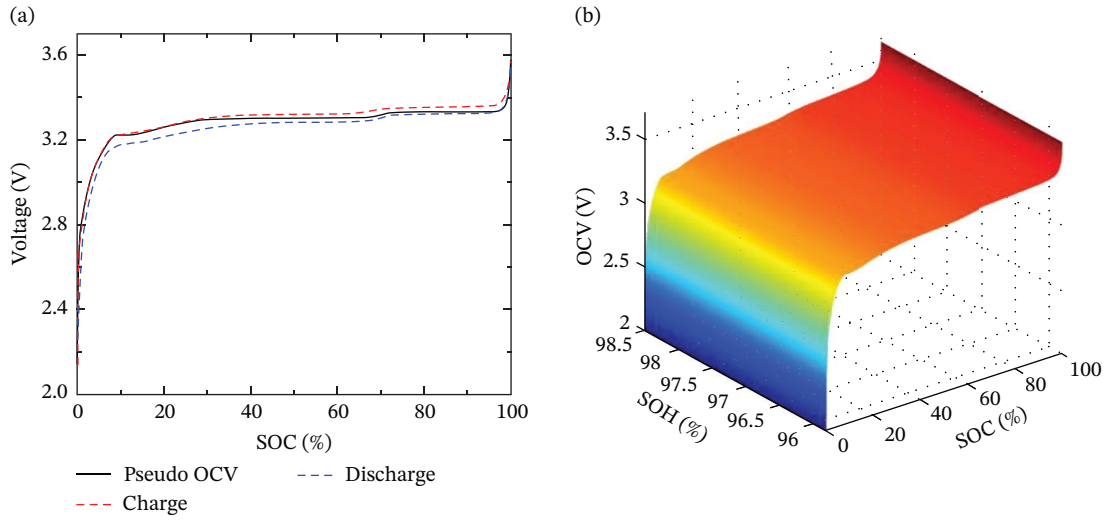

FIGURE 2 | (a) Pseudo-OCV estimation method and (b) pseudo-OCV look-up table.

ijer, 2026, 1, Downloaded from https://onlinelibrary.wiley.com/doi/10.1155/er/7965949 by Hanyang University Library, Wiley Online Library on [01/11/2026]. See the Terms and Conditions (https://onlinelibrary.wiley.com/terms-and-conditions) on Wiley Online Library for rules of use; OA articles are governed by the applicable Creative Commons License

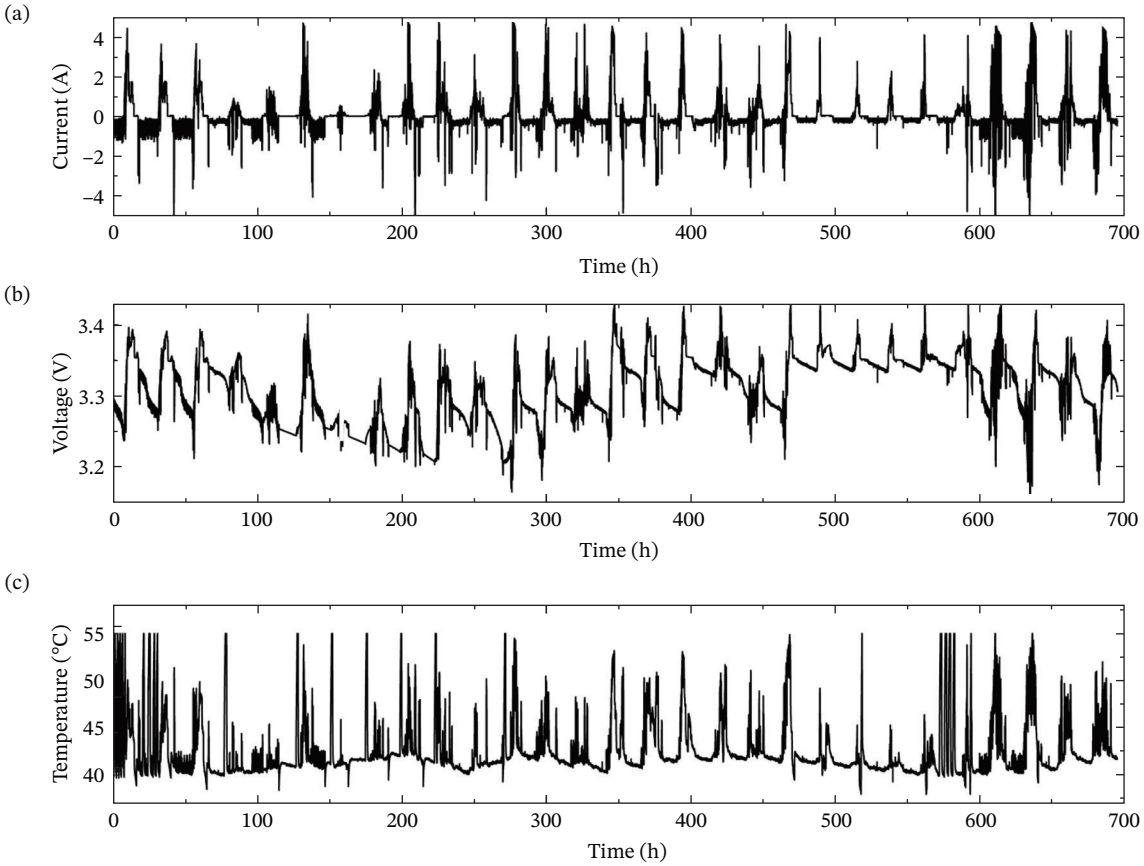

FIGURE 3 | (a) Current, (b) potential, and (c) temperature of the operating condition of the BESS at the European site during March.

3 | Proposed Framework for SOC Estimation

This study proposes an integrated framework for the SOC estimation of an LFP battery module. The proposed framework robustly estimates the SOC under various operational temperatures in three phases:

1. The EECM is proposed to accurately represent the complex electrochemical and thermal behaviors of the LFP battery module (black box (a) in Figure 4). This model is deployed in the UKF as a reference model for estimating the potential and corresponding SOC because the UKF is a model-based method [48]. The EECM addresses inherent challenges in the LFP battery module, including the SOC inconsistency among cells and the strong dependency of the OCV on temperature.
2. An offline database construction and comprehensive parameter identification are performed (red box (b) in Figure 4). The OCV LUT is constructed as a function of both the SOC and temperature because the OCV LUT plays a critical role in the EECM to accurately represent the thermodynamics of the LFP module [49] (Figure 4b-①). The parameters used in the EECM are initialized by addressing a least square method (Figure 4b-②) because appropriate parameters consider the internal resistance and polarization characteristics of the LFP module. Further, BO is employed to systematically tune the parameters of the Kalman filter (Figure 4b-③). This optimization ensures the robustness and adaptability of the filter under real-world conditions with large temperature variations and stochastic loads.
3. The SOC is estimated in real time (blue box (c) in Figure 4). The measured potential and current are fed into the dual-UKF framework. The first filter recursively updates the EECM parameters to reflect the nonlinear dynamics of the LFP module. Subsequently, the second UKF estimates the SOC by analyzing the model-based potential $\widehat{V_k}$ and measured potential $V_{m,k}$. The architecture of the dual-UKF enables the proposed framework to provide the internal states of the LFP module and time-varying parameters, securing high accuracy for SOC estimation.

3.1 | EECM

An EECM is proposed to accurately estimate the potential of the 2s4p LFP battery module considering SOC inconsistency (Figure 5a). The proposed method accounts for the complex electrochemical behaviors of the LFP battery module, including the OCV, resistance effect, and hysteresis effect, which are conventional issues in an LFP module originating from both nonlinear electrochemical reactions and diffusion [50]. The LFP module includes four parallel cells connected to the positive tab and four connected to the negative tab. This configuration results in a slight difference in the local SOC because of minor variations in the internal impedance and capacity. This concern can be addressed by adopting an average OCV because this method can represent this macroscopic behavior without a computational burden (Figure 5b). Hence, the proposed EECM effectively replicates the dynamic characteristics of the LFP module of interest. The continuous dynamics of the EECM must be discredited into a canonical

ijer, 2026, 1, Downloaded from https://onlinelibrary.wiley.com/doi/10.1155/er/7965949 by Hanyang University Library, Wiley Online Library on [01/11/2026]. See the Terms and Conditions (https://onlinelibrary.wiley.com/terms-and-conditions) on Wiley Online Library for rules of use; OA articles are governed by the applicable Creative Commons License

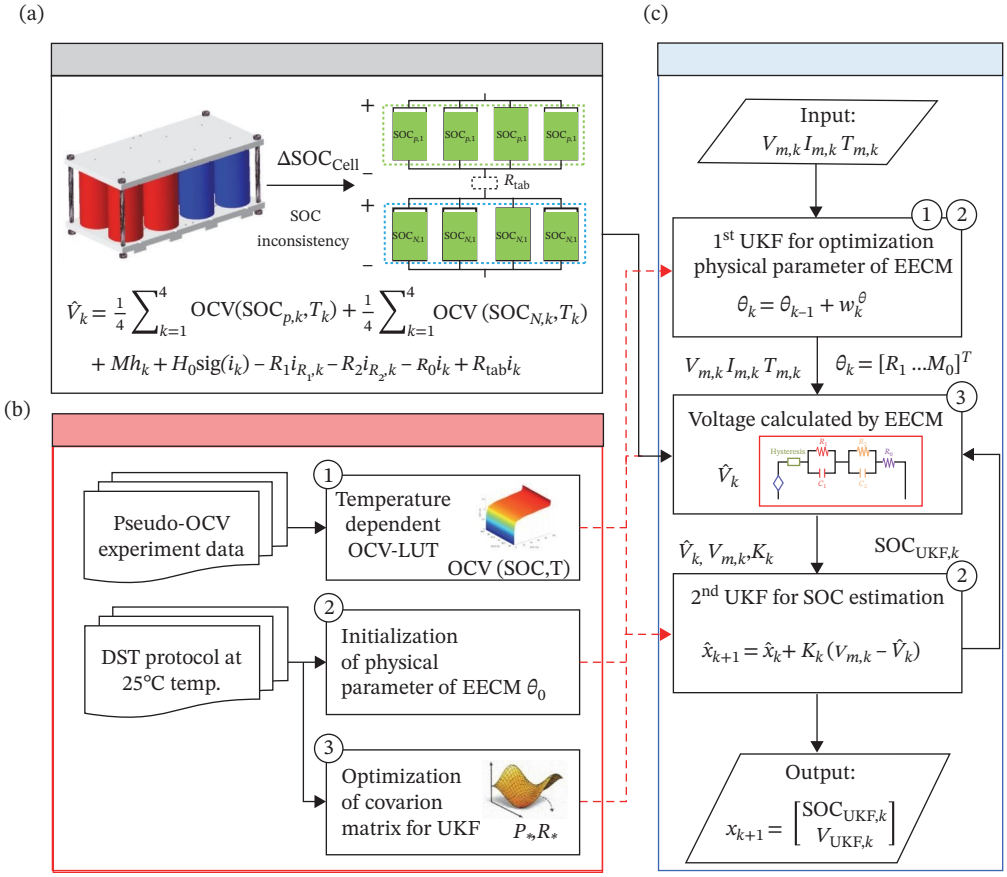

FIGURE 4 | Integrated framework of the SOC estimation. (a) Enhanced equivalent circuit model (EECM). (b) Parameter preparation with offline dataset. (c) Real-time estimation algorithm.

controllable form (CCF) because the dual-UKF requires a state-space system in the discrete-time domain. The process for obtaining the CCF state-space equations is presented in Figure 5c. The input vector u_k and output vector y_k at time step k are defined as

$$\begin{aligned} u_k &= [i_k, T_k]^T, \\ y_k &= V_k, \end{aligned} \tag{1}$$

where i_k, T_k, and V_k represent the current imposed, module temperature, and potential of the module, respectively. The state vector x_k is defined to include the SOC and hysteresis potential h_k as

$$x_k = \left[\mathrm{SOC}_k, h_k, i_{R_1,k}, i_{R_2,k}\right]^T, \tag{2}$$

where $i_{R_1,k}$ and $i_{R_2,k}$ represent the polarization currents across RC branches in Figure 5a for considering the internal dynamics of both polarization effects and SOC deviation. The discrete-time evolution of decoupled currents is governed by the analytical solution of first-order differential equations as

$$\begin{aligned} i_{R_1,k+1} &= \exp\left(\frac{-\Delta t}{\tau_1}\right) i_{R_1,k} + \left(1 - \exp\left(\frac{-\Delta t}{\tau_1}\right)\right) i_k, \\ i_{R_2,k+1} &= \exp\left(\frac{-\Delta t}{\tau_2}\right) i_{R_2,k} + \left(1 - \exp\left(\frac{-\Delta t}{\tau_2}\right)\right) i_k, \end{aligned} \tag{3}$$

where $\tau_1 = R_1 C_1$ and $\tau_2 = R_2 C_2$ represent the time constants of the two RC branches. τ_1 represents the slow time constant associated with concentration polarization of diffusion effects [51]. In contrast, τ_2 represents the fast time constant associated with electrochemical polarization because of charge transfer [52]. LIBs exhibit a significant potential difference between the charge and discharge OCV, even at the same SOC [53], resulting in substantial errors in SOC estimation. This concern is addressed by adopting the hysteresis potential $V_{\mathrm{hys},j}$ as a superposition of two distinct components, that is, instantaneous hysteresis and dynamic hysteresis, as

$$V_{\mathrm{hys}} = H_0 \mathrm{sig}(i_k) + M h_k, \tag{4}$$

where H_0, M, and h_k confirm the magnitude of this instantaneous potential difference, maximum polarization amplitude of the dynamic hysteresis, and hysteresis level relative to the major loop, respectively. The first term in $H_0 \mathrm{sig}(i_k)$ represents the immediate potential jump observed when the direction of the current changes. Therefore, the term accounts for the rapid shift in the equilibrium potential at the electrode surface. The second term in Mh_k describes the transient behavior of the hysteresis potential [54]. The evolution of the hysteresis state h_k is governed by a differential equation with respect to the imposed current as

$$h_{k+1} = \exp(-|\gamma i_k|\Delta t) h_k + (1 - \exp(-|\gamma i_k|\Delta t)) i_k, \tag{5}$$

where γ represents the hysteresis decay rate constant. This determines how quickly the potential transitions from the charge curve to the discharge curve. Finally, the complete state-space equation is constructed as

ijer, 2026, 1, Downloaded from https://onlinelibrary.wiley.com/doi/10.1155/er/7965949 by Hanyang University Library, Wiley Online Library on [01/11/2026]. See the Terms and Conditions (https://onlinelibrary.wiley.com/terms-and-conditions) on Wiley Online Library for rules of use; OA articles are governed by the applicable Creative Commons License

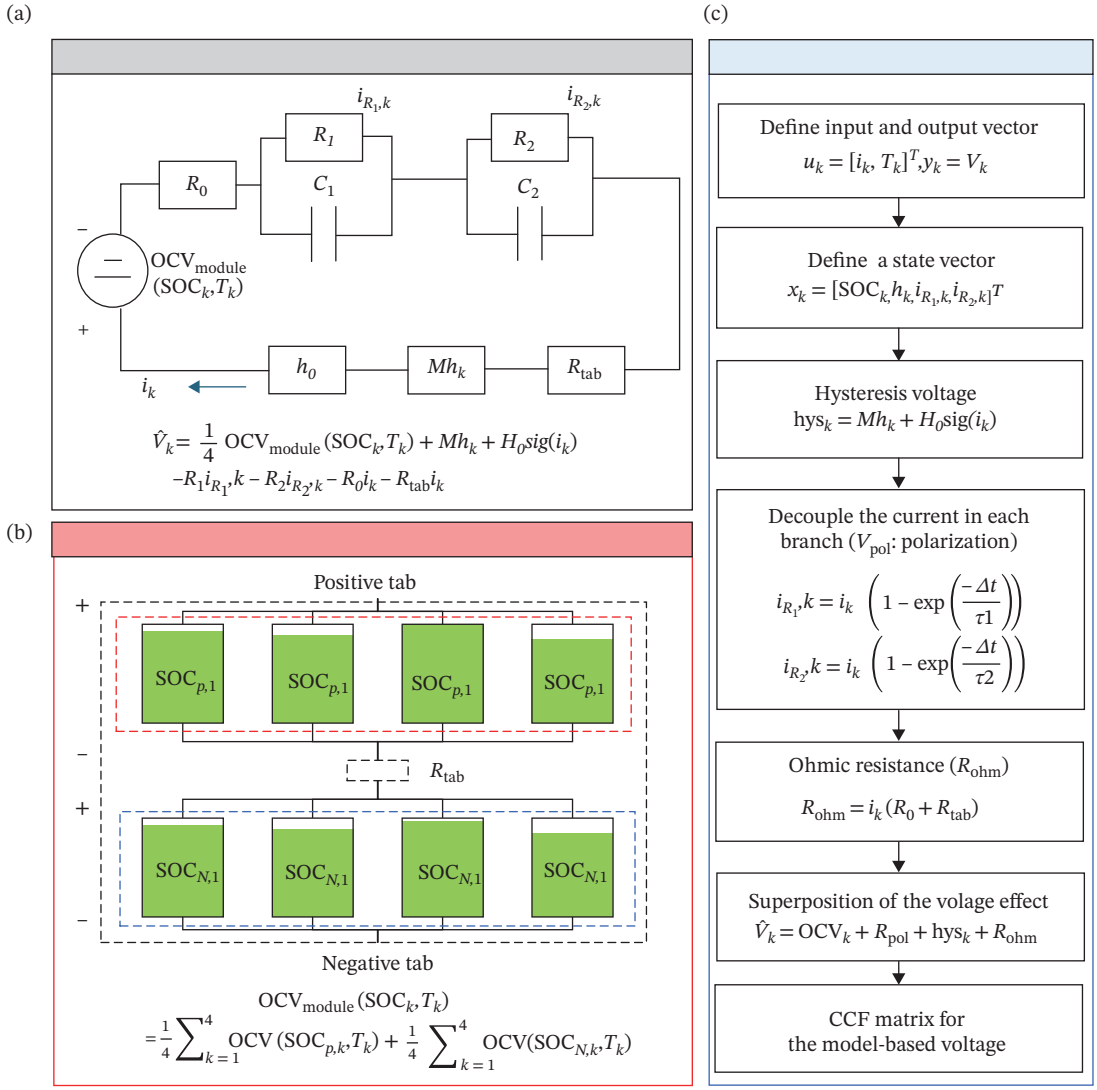

FIGURE 5 | (a) Enhanced equivalent circuit model (EECM), (b) average-OCV, and (c) canonical controllable form (CCF) for EECM.

$$x_{k+1} = \begin{bmatrix} 1 & 0 & 0 & 0 \\ 0 & \exp\left(-\frac{\eta}{\gamma|i_k|\Delta t}\right) & 0 & 0 \\ 0 & 0 & \exp\left(-\frac{\Delta t}{\tau_1}\right) & 0 \\ 0 & 0 & 0 & \exp\left(-\frac{\Delta t}{\tau_2}\right) \end{bmatrix} x_k + \begin{bmatrix} \frac{\eta \Delta t}{\gamma Q} \\ \left(1 - \exp\left(-\frac{\eta}{\gamma|i_k|\Delta t}\right)\right)\mathrm{sgn}(i_k) \\ \left(1 - \exp\left(-\frac{\Delta t}{\tau_1}\right)\right) \\ \left(1 - \exp\left(-\frac{\Delta t}{\tau_2}\right)\right) \end{bmatrix}, \tag{6}$$

where Q and η represent the nominal capacity of the module and Coulombic efficiency. The CCF of the EECM is formulated by considering the OCV, hysteresis dynamics, and decoupled polarization currents. This state-space formulation enables the UKF to directly capture electrochemical characteristics. Hence, the macroscopic potential V_k of the EECM is expressed for the LFP module considering the 2s4p configuration as

$$V_k = \frac{1}{4}\sum_{k=1}^{4} \mathrm{OCV}\left(\mathrm{SOC}_{P,k}, T_k\right) + \frac{1}{4}\sum_{k=1}^{4} \mathrm{OCV}\left(\mathrm{SOC}_{N,k}, T_k\right) + Mh_k + H_0 \mathrm{sig}(i_k) - R_1 i_{R_1,k} - R_2 i_{R_2,k} - R_0 i_k + R_{\mathrm{tab}} i_k, \tag{7}$$

where $\mathrm{SOC}_{P,j}$, $\mathrm{SOC}_{N,j}$, R_0, and R_{tab} represent SOC values sampled at four evenly distributed points on the positive and negative electrodes, bulk resistance, and tab resistance, respectively. The averaged OCV approximates the distributed electrode-level SOC behavior by considering the SOC inconsistency effect (Figure 5b) [55]. The $R_{\mathrm{tab}} i_k$ represents the contact-resistance contribution of the tab, which is relevant to high-current operation and thermal sensitivity. Thus, the EECM defines a complete nonlinear state-space representation for recursive SOC estimation.

3.2 | Parameter Preparation With the Constructed Dataset

Offline optimization is achieved by addressing BO to systematically identify parameters used in the EECM and dual-UKF.

ijer, 2026, 1, Downloaded from https://onlinelibrary.wiley.com/doi/10.1155/er/7985949 by Hanyang University Library, Wiley Online Library on [01/11/2026]. See the Terms and Conditions (https://onlinelibrary.wiley.com/terms-and-conditions) on Wiley Online Library for rules of use; OA articles are governed by the applicable Creative Commons License

TABLE 2 | Initial guess and boundary ranges of both EECM parameters for optimization and the dual-UKF hyperparameters.

Parameter	Description	Initial guess	Boundary [Min, Max]	Optimized value	Unit	Source
R_0	Ohmic resistance	0.05	[0.010, 0.100]	0.0130	Ω	[56]
R_1	Polarization resistance 1	0.02	[0.001, 0.100]	0.0182	Ω	[56]
R_2	Polarization resistance 2	0.02	[0.001, 0.100]	0.0142	Ω	[56]
R_{tab}	Tab resistance	0.005	[0.001, 0.020]	0.003	Ω	[57]
C_1	Polarization capacitance 1	1500	[100, 5000]	120.44	F	[56]
C_2	Polarization capacitance 2	2500	[100, 8000]	33.95	F	[56]
M_0	Hysteresis magnitude	0.03	[0.001, 0.100]	0.0956	V	[57]
H_0	Hysteresis factor	0.5	[0.001, 1.000]	0.0063	—	[57]
α	Spread parameter	1×10^{-3}	$[1\times10^{-4}, 1]$	0.1	—	[56]
β	Scaling parameter	2	[1.0, 4.0]	4	—	[56]
κ	Distribution information	0	[0.0, 10.0]	9	—	[56]
Q_*	Process noise covariance	1×10^{-6}	$[1\times10^{-8}, 1\times10^{-4}]$	1×10^{-5}	—	[57]
R_*	Measurement noise covariance	1×10^{-4}	$[1\times10^{-6}, 1\times10^{-2}]$	1×10^{-3}	—	[57]

This optimization initializes EECM parameters and estimates filter parameters in the dual-UKF because this optimization plays an important role in ensuring the accurate and robust performance of the proposed method for SOC estimation. The DST data acquired at 25°C are utilized as a reference baseline because the DST profile effectively characterizes the electrochemical behaviors of the LFP module by employing a series of rapid charge and discharge pulses with varying amplitudes. Pulse currents effectively excite the complex dynamic characteristics of the LFP module of interest, including Ohmic drops, charge–transfer polarization, and diffusion processes [54].

The initial EECM parameters were estimated from the DST data because the EECM parameters were recursively updated with the first UKF in the proposed framework. The recursive parameter update accounts for time-varying nonlinearities and environmental fluctuations of battery responses because the adaptive structure considers temperature-dependent polarization that is not represented in the OCV LUT [55]. Therefore, the adaptively updated parameter guarantees the robustness and reliability of the SOC estimation under various operational conditions. Eight parameters ($\theta_0 = [R_{0,\text{init}}, R_{1,\text{init}}, R_{2,\text{init}}, R_{\text{tab,init}}, C_{1,\text{init}}, C_{2,\text{init}}, M_{0,\text{init}}, H_{0,\text{init}}]^T$) addressed in the EECM are estimated to replicate the electrochemical characteristics of the LFP module. Both initial guess and boundary ranges between the minimum and maximum should be appropriately established for each parameter to ensure physical feasibility and convergence. Therefore, we identified a physically reasonable region for each parameter based on a literature survey of the LFP module to avoid unrealistic values [56, 57]. Detailed constraints for the optimization are listed in Table 2. The objective function addressed in the initialization minimizes the error between the potential predicted by the EECM and the actual measured potential as

$$\text{argmin}\left[\sum_{n=1}^{N}\left(\frac{V_n^{\text{pred}} - V_n^{\text{exp}}}{V_n^{\text{pred}}}\right)^2\right], \tag{8}$$

where superscripts pred and exp represent the predicted results from the proposed method and experimental results, respectively, and the subscript n denotes the step time with an interval of 1 s. For brevity, EECM parameters were initialized via BO, as described in Appendix B.

Optimization is employed to calibrate both noise covariance matrices Q_*, measurement noise covariance R_*, and distribution parameters used in the dual-UKF because the performance of the UKF is intrinsically affected by the precise calibration of these parameters. The optimization of both noise covariance matrices Q_* and measurement noise covariance R_* directly affects both the convergence and minimization of estimation errors. The Q_* represent the uncertainty of the physical dynamics of the EECM, while the R_* represents the statistical characteristics of the sensor noise and measurement errors [58]. An imbalance between Q_* and R_* results in an inaccurate SOC estimation because of unreasonable information regarding errors. Therefore, the systematic optimization of these parameters is essential for securing the robustness of the SOC estimation framework. The distribution parameters including the spread parameter α, scaling parameter β, and distribution information κ should be optimized to determine the sigma point distribution of the dual-UKF. The UKF employs a deterministic sampling technique, UT, to provide a set of deterministic sigma points that represent the mean and covariance of the state distribution. The UKF approximates the probability distribution of the state variable by searching for a minimal set of deterministic sample points considering the nonlinear characteristics with the distribution parameters based on the UT [59]. Therefore, distribution parameters should be optimized to determine the sigma point distribution and ensure the adaptability of the proposed method to stochastic loads [32]. The BO was deployed to determine the optimal parameters of the dual-UKF, similar to the initial parameter identification for the EECM. The objective function of the optimization minimizes the potential error over the DST profile in Equation (8). This objective function ensures the high performance and stability of the dual-UKF under operational conditions.

ijer, 2026, 1, Downloaded from https://onlinelibrary.wiley.com/doi/10.1155/er/7903949 by Hanyang University Library, Wiley Online Library on [01/11/2026]. See the Terms and Conditions (https://onlinelibrary.wiley.com/terms-and-conditions) on Wiley Online Library for rules of use; OA articles are governed by the applicable Creative Commons License

3.3 | Real-Time SOC Estimation

The proposed method uses a dual-loop architecture that simultaneously estimates the SOC and updates the EECM model parameters. A detailed flowchart of this process is shown in Figure 6. The input vector is defined as $u_k = [V_{m,k}, I_{m,k}, T_m,]$ because the measurements are the current, potential, and temperature. The measured terminal potential $V_{m,k}$ served as the observation variable in the dual-UKF. The estimation process is divided into two sequential stages: first and second UKFs. The first UKF (parameter-UKF) updates the model parameters of the EECM, and the second UKF (state-UKF) estimates the SOC and potential. Both filters utilize the same optimized hyperparameters of process noise covariance Q_*, measurement noise covariance R_*, and scaling parameters of α, β, and κ, which are preliminarily determined via BO.

The first UKF identifies the time-varying parameters of the EECM in real time. Adaptive parameters minimized the error between the potential predicted by the EECM and the measured potential caused by temperature fluctuations. The parameter state vector θ_k includes the critical circuit components defined in the EECM as

$$\theta_k = \left[R_{0,k}, R_{1,k}, R_{2,k}, R_{\text{tab},k}, C_{1,k}, C_{2,k}, M_{0,k}, H_{0,k}\right]^T. \tag{9}$$

The recursive update of these model parameters in the EECM is governed by the Kalman gain as

$$\theta_{k+1} = \theta_k + K_{\theta,k}\left(V_{m.k} - \widehat{V}_{k|k-1}\right), \tag{10}$$

where $K_{\theta,k}$ and $\widehat{V}_{k|k-1}$ represent the Kalman gain and model-predicted potential based on the EECM. The residual potential $V_{m.k} - \widehat{V}_{k|k-1}$ represents the difference between the potential measured from the LFP module $V_{m.k}$ and the model-predicted potential $\widehat{V}_{k|k-1}$ using the prior parameters at the $k-1$th step. The Kalman gain $K_{\theta,k}$ is a weighting function that optimizes the effect of updating parameters for minimizing the prediction error for each time step [58]. Therefore, the Kalman gain $K_{\theta,k}$ optimally weighs the parameter update as

$$K_{\theta,k} = P_{\theta,k}\, S_{\theta,k}, \tag{11}$$

where $P_{\theta,k}$ and $S_{\theta,k}$ represent the cross-covariance between the parameter state vector θ_k and the model-predicted potential and

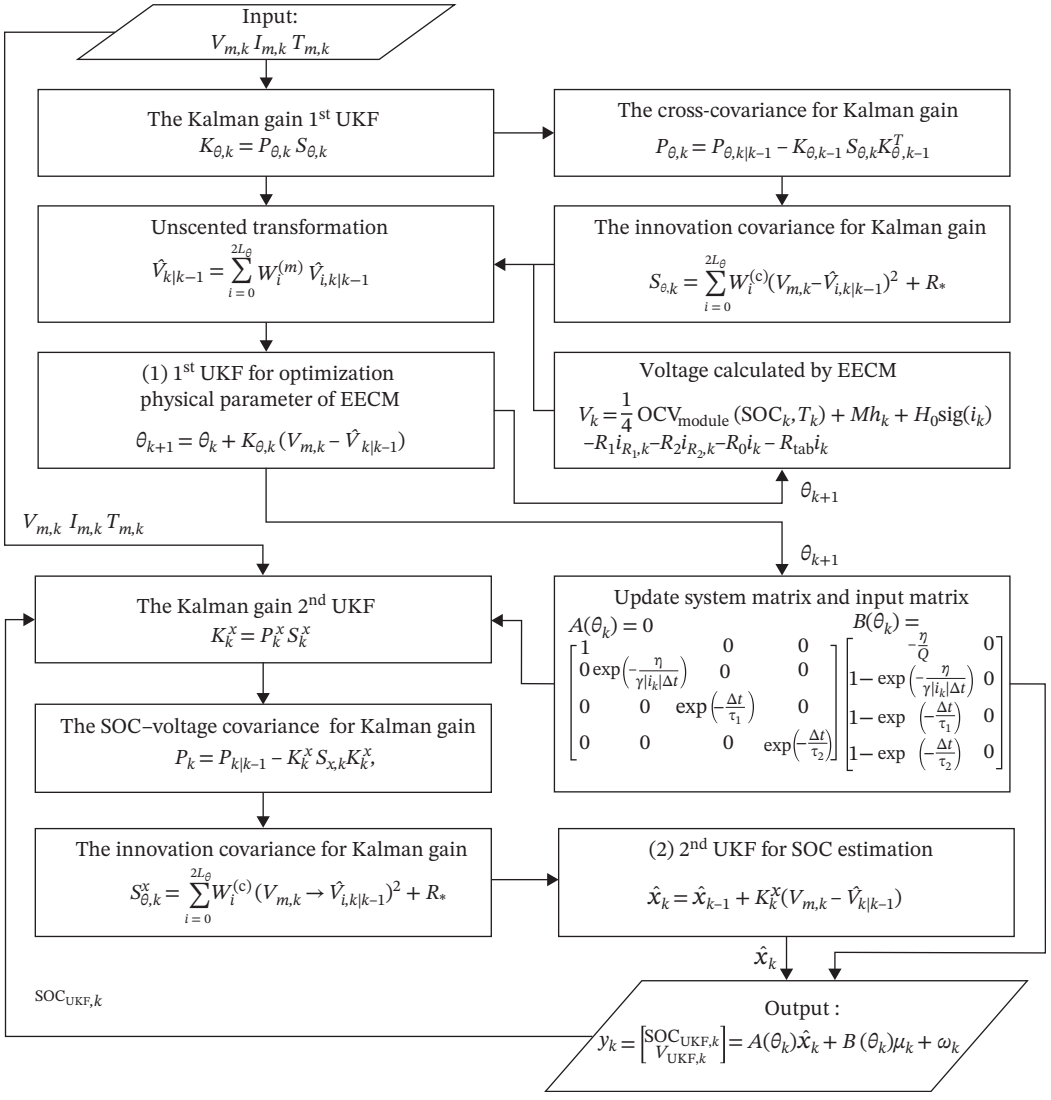

FIGURE 6 | Flowchart of the real-time SOC estimation.

ijer, 2026, 1, Downloaded from https://onlinelibrary.wiley.com/doi/10.1155/er/7965949 by Hanyang University Library, Wiley Online Library on [01/11/2026]. See the Terms and Conditions (https://onlinelibrary.wiley.com/terms-and-conditions) on Wiley Online Library for rules of use; OA articles are governed by the applicable Creative Commons License

innovation covariance. A large value in the cross-covariance $P_{\theta,k}$ indicates that the model-predicted potential is highly sensitive to variations in specific EECM parameters, thereby resulting in a larger weight to innovate for updating those parameters [59]. Therefore, the cross-covariance $P_{\theta,k}$ is updated as

$$P_{\theta,k} = P_{\theta,k|k-1} - K_{\theta,k-1} S_{\theta,k} K_{\theta,k-1}^T, \tag{12}$$

where $P_{\theta,k}$ and $P_{\theta,k|k-1}$ represent the posterior and prior parameter covariance matrices. The term $K_{\theta,k-1} S_{\theta,k} K_{\theta,k-1}^T$ represents the information gain of the cross-covariance. Therefore, Equation (12) increases the confidence level in the adaptively updated parameters by subtracting this term $K_{\theta,k-1} S_{\theta,k} K_{\theta,k-1}^T$ from prior covariance [59]. Interestingly, the innovation covariance $S_{\theta,k}$ affects the Kalman gain $K_{\theta,k}$ and cross-covariance $P_{\theta,k}$. The innovation covariance $S_{\theta,k}$ is treated as a normalization factor, which is proportional to the total uncertainty, for preventing overfitting to Gaussian noise [32]. The total uncertainty associated with the model-predicted potential is quantified by the innovation covariance $S_{\theta,k}$, which is computed as

$$S_{\theta,k} = \sum_{i=0}^{2L_\theta} W_i^{(c)} \left(V_{m,k} - \widehat{V}_{i,k|k-1} \right)^2 + R_*, \tag{13}$$

where $W_i^{(c)}$, L_θ, $\widehat{V}_{i,k|k-1}$, and R_* represent the covariance weights associated with the UT, dimension of the parameter state vectors, potential prediction corresponding to the ith sigma point, and measurement noise covariance, respectively. The first term $W_i^{(c)} (V_{m,k} - \widehat{V}_{i,k|k-1})^2$ accounts for the variance of the model-predicted potential in UT. The measurement noise covariance R_* considers sensor noise and unmodelled errors [32]. R_* is a critical hyperparameter optimized via the BO to accurately reflect the sensor characteristics [60]. The $\widehat{V}_{i,k|k-1}$ propagates sigma points through the EECM based on the UT. The UT generates a minimal set of deterministic sigma points for the mean and covariance of the physical model, which enables accurate propagation through nonlinear mappings without linearization [61]. The UT utilizes several samples and the model calculation average value of the sample as the model calculation value is similar to the linearized Jacobian employed for the model calculation value in the EKF [60]. The mean potential predicted by the UT is obtained as

$$\widehat{V}_{k|k-1} = \sum_{i=0}^{2L_\theta} W_i^{(m)} \, \widehat{V}_{i,k|k-1}. \tag{14}$$

The weights $W_i^{(m)}$ are determined by the distribution parameters (α, β, and κ) for each sigma point. The model-predicted potential is calculated at a single point by inserting the parameter variation into the EECM as

$$\widehat{V}_{i,k|k-1} = g\left(\widehat{x}_{k|k-1}, u_k, \widehat{\theta}_k \right), \tag{15}$$

where $g(\cdot)$ indicates that the function of the EECM. Equation (15) generates scattered points of the model-predicted potential $\widehat{V}_{i,k|k-1}$ that maps into uncertainty through the EECM. UT determines independent variables to sample, given that the resulting sampled data rely on these variables [62]. This study employs the independent variable as model parameter $\widehat{\theta}_k$, which considers the effect of the varied parameter. The independent parameters of the EECM are modeled as a random-walk process at each step assuming that parameter changes are negligible over a single sampling interval as

$$\widehat{\theta}_k = \widehat{\theta}_{k-1} + \omega_k^\theta, \omega_k^\theta \sim N(0, Q_*), \tag{16}$$

where $\widehat{\theta}_k$, $\widehat{\theta}_{k-1}$, Q_*, and ω_k^θ represent the independent parameters of the EECM, parameter estimates of the previous time steps, covariance matrix, and process noise, respectively. The independent parameters $\widehat{\theta}_k$ are modeled as a zero-mean Gaussian distribution with a covariance matrix Q_*, which is recommended for parameter estimation with UKF [63].

The second UKF estimates both the SOC and potential of the LFP module using the updated parameters θ_k from the first UKF. The state vector x_k at time step k is defined to consider both the SOC and polarization effects across the two RC branches and the hysteresis state. The potential can be predicted using EECM by utilizing the values of the second, third, and fourth columns of the state vector $\widehat{x}_k$ as

$$\widehat{x}_k = \begin{bmatrix} \mathrm{SOC}_k \\ h_k \\ i_{1,k} \\ i_{2k} \end{bmatrix}. \tag{17}$$

The second UKF operates the UT by propagating a matrix of sigma points through nonlinear system dynamics. The posterior state vector $\widehat{x}_k$ is obtained by adding the weighted innovation to the a priori estimate $\widehat{x}_{k-1}$. The innovation corrects the potential based on the difference between the observed and predicted potentials as

$$\widehat{x}_k = \widehat{x}_{k-1} + K_k^x \left(V_{m,k} - \widehat{V}_{k|k-1} \right), \tag{18}$$

where K_k^x represents the Kalman gain for the second UKF and $K_k^x = [k_1, \ k_2, \ k_3, \ k_4]^T$. The first Kalman gain factor k_1 quantifies how the residual potential should be tuned as an SOC mismatch, enabling effective SOC correction. The second Kalman gain factor k_2 determines the extent to which the potential mismatch is attributed to the hysteresis state. The third and fourth Kalman gain factors k_3 and k_4 correspond to the first and second polarization states, respectively, which are transient behaviors that enable the filter to correct polarization dynamics. In addition, the Kalman gain for the second UKF is expressed as

$$K_k^x = P_k^x S_k^x, \tag{19}$$

where P_k^x and S_k^x represent the SOC potential covariance and innovation variance for the second UKF, respectively. The Kalman gain matrix acts as a projection matrix, mapping the potential error from the observation space to the state space. Therefore, the SOC potential covariance can be obtained as

$$P_k = P_{k|k-1} - K_k^x S_{x,k} K_k^{xT}. \tag{20}$$

Equation (20) ensures that uncertainty decreases dominantly along state directions that are well-informed by the measured potential at step k. The total uncertainty associated with the model-predicted potential is quantified by the innovation covariance $S_{\theta,k}^x$, which is computed as

ijer, 2026, 1, Downloaded from https://onlinelibrary.wiley.com/doi/10.1155/er/7965949 by Hanyang University Library, Wiley Online Library on [01/11/2026]. See the Terms and Conditions (https://onlinelibrary.wiley.com/terms-and-conditions) on Wiley Online Library for rules of use; OA articles are governed by the applicable Creative Commons License

$$S^x_{\theta,k} = \sum_{i=0}^{2L_\theta} W_i^{(c)} \left(V_{m,k} - \widehat{V}_{i,k|k-1}\right)^2 + R_*, \tag{21}$$

where $W_i^{(c)}$, L_θ, $\widehat{V}_{i,k|k-1}$, and R_* represent the covariance weights associated with the UT. The Kalman gain for the second UKF as $K_k^x = [k_1,\ k_2,\ k_3,\ k_4]^T$ is automatically updated over time, reflecting both the local sensitivity of the potential to each state at the current operating point and the confidence level determined by the innovation covariance $S^x_{\theta,k}$.

The output y_k of the second UKF is obtained using the continuous-time governing equations of the EECM, which are discretized into a state-space matrix form. The output y_k of the second UKF for both the SOC and potential estimation is formulated as

$$y_k = \begin{bmatrix} \mathrm{SOC}_{\mathrm{UKF},k} \\ V_{\mathrm{UKF},k} \end{bmatrix} = \boldsymbol{A}(\theta_k)\widehat{x}_k + \boldsymbol{B}(\theta_k)u_k + \omega_k, \tag{22}$$

where $\boldsymbol{A}(\theta_k)$, $\boldsymbol{B}(\theta_k)$, and ω_k represent the system matrix, input matrix, and process noise matrix, respectively. The decoupled solution of the differential equations based on the EECM is expressed as

$$\boldsymbol{A}(\theta_k) = \begin{bmatrix} 1 & 0 & 0 & 0 \\ 0 & \exp\left(-\dfrac{\eta}{\gamma|i_k|\Delta t}\right) & 0 & 0 \\ 0 & 0 & \exp\left(-\dfrac{\Delta t}{\tau_1}\right) & 0 \\ 0 & 0 & 0 & \exp\left(-\dfrac{\Delta t}{\tau_2}\right) \end{bmatrix} +, \tag{23}$$

$$\boldsymbol{B}(\theta_k) = \begin{bmatrix} -\dfrac{\eta}{Q} & 0 \\ 1 - \exp\left(-\dfrac{\eta}{\gamma|i_k|\Delta t}\right) & 0 \\ 1 - \exp\left(-\dfrac{\Delta t}{\tau_1}\right) & 0 \\ 1 - \exp\left(-\dfrac{\Delta t}{\tau_2}\right) & 0 \end{bmatrix}. \tag{24}$$

The architecture of the dual-UKF enables the proposed framework to provide the internal states of the LFP module and time-varying parameters, ensuring high accuracy for SOC estimation. The details of the real estimations are outlined in Algorithm 1.

ALGORITHM 1 | Pseudo-code for real-time SOC estimation.

1 Input real-time measurements in each step ($V_{m,k}$, $I_{m,k}$, and $T_{m,k}$)

2 Parameter state vector θ_k and state vector for SOC estimation x_k

3 Perform the UT $\sum_{i=0}^{2L_\theta} W_i^{(c)} (V_{m,k} - \widehat{V}_{i,k|k-1})^2$

4 Random walk regularizes parameters $\widehat{\theta}_k = \widehat{\theta}_{k-1} + \omega_k^\theta$, $\omega_k^\theta \sim N(0, Q_*)$

5 Update the innovation covariance $S_{\theta,k}$

6 Update the cross-covariance $P_{\theta,k}$

7 Update the Kalman gain $K_{\theta,k}$

8 Recursive update parameters θ_{k+1}

9 Steps 3–6 are repeated for the SOC estimation using the first UKF

10 Update the system matrix and the input matrices $A(\theta_k)$ and $B(\theta_k)$

11 Update the posterior state vector $\widehat{x}_k = \widehat{x}_{k-1} + K_k^x(V_{m,k} - \widehat{V}_{k|k-1})$

12 Obtain the output y_k of the second UKF $y_k = \begin{bmatrix} \mathrm{SOC}_{\mathrm{UKF},k} \\ V_{\mathrm{UKF},k} \end{bmatrix}$

4 | Results and Discussion

This section presents a comprehensive evaluation of the proposed framework for the SOC estimation through an in-depth discussion. The validation process is structured into four parts: identifying the parameters for the proposed method through BO; quantitatively evaluating the accuracy of the SOC estimation, convergence speed of the SOC, and potential estimation under three different dynamic driving schedules; investigating the robustness of the proposed method under varying ambient temperatures and confirming its thermal adaptability; and determining the practical applicability of the proposed method using real-world stochastic operational data from the BESS dataset. All computations were executed on a high-performance workstation equipped with an Intel i9-11900 processor, NVIDIA GeForce GTX 3090 GPU, and 32 GB of DDR4 RAM to ensure computational efficiency during validation. The proposed method is implemented using MATLAB 2023a.

4.1 | Parameter Identification

The model parameters deployed in the proposed framework are obtained from the experiments (Table 2). The potential profile in the DST cycle acquired at 25°C is utilized as a reference baseline. This is because the electrochemical behaviors of the LFP module are characterized by employing DST profiles with a series of rapid charge and discharge pulses with varying amplitudes. BO was used for parameter optimization. The objective function in the initialization minimizes the error between the model-predicted potential and the measured potential in Equation (8). The detailed constraints for the optimization are listed in Table 2. This study identifies a physically reasonable boundary for each parameter based on a literature survey of the LFP module to avoid unrealistic values [56, 57].

The validity of the optimization is visually corroborated in Figure 7. The model-predicted potential accurately matches the measured potential during repeated DST cycles, as shown in Figure 7a. The magnified view from 200 to 260 min (Figure 7b) indicates that the proposed method accurately tracks the rapid transient responses induced by the dynamic current pulses of the DST cycle. This observation confirms that the estimated parameters deployed in the proposed method accurately replicate the instantaneous potential drops governed by Ohmic resistance and the potential recovery driven by polarization effects [64]. The quantitative error between the model-predicted and measured potentials is analyzed by calculating the root-mean-square

ijer, 2026, 1, Downloaded from https://onlinelibrary.wiley.com/doi/10.1155/er/7965949 by Hanyang University Library, Wiley Online Library on [01/11/2026]. See the Terms and Conditions (https://onlinelibrary.wiley.com/terms-and-conditions) on Wiley Online Library for rules of use; OA articles are governed by the applicable Creative Commons License

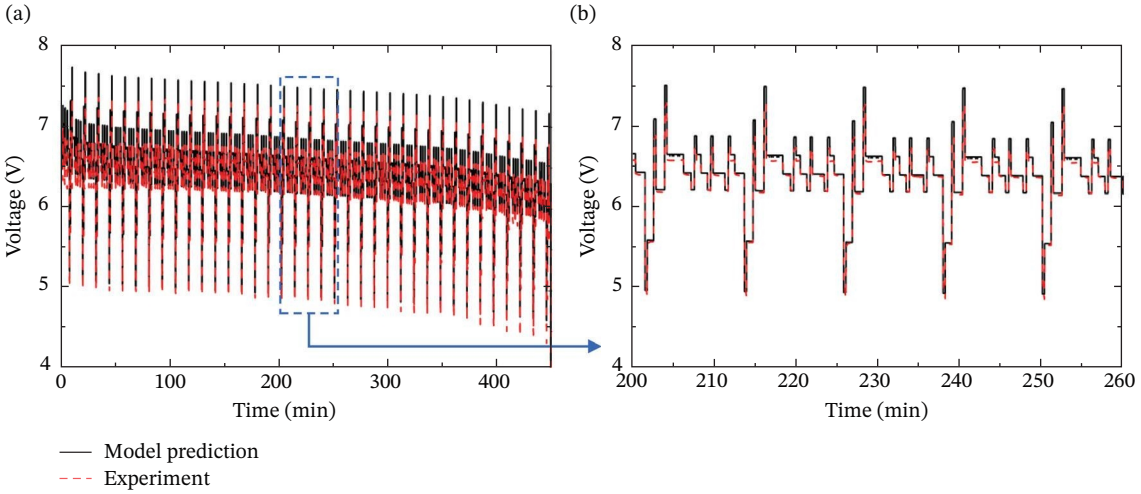

FIGURE 7 | (a) Potential estimation for the DST driving cycle and (b) magnified view from 200 to 260 min.

error (RMSE). The potential RMSE value was 0.0015 V for the DST cycles of the LFP module, suggesting that parameters deployed in the proposed method accurately replicated the electrochemical dynamics of the LIB module of interest. Thus, the objective function effectively optimized the parameters of the proposed method.

The model parameters optimized in the experiments are also summarized in Table 2. Accurate parameter identification is critical for SOC estimation because the accuracy of the SOC estimation depends on the fidelity of the deployed model and convergence performance of the dual-UKF. Consequently, a detailed quantitative analysis is conducted to verify the physical consistency of each identified parameter and ensure that it accurately reflects the inherent electrochemical characteristics of the LFP module.

The model parameters of the EECM represent the internal electrochemical dynamics of the LFP module. The identified parameters are physically validated by analyzing the time constants $\tau = RC$ of the two RC branches for the EECM. Based on the optimized values, the time constant of the first branch τ_1 is calculated at 2.19 s, while that of the second branch τ_2 is significantly smaller at 0.48 s. τ_1 is ~4.5 times larger than τ_2; this distinct separation on the time scale aligns well with the electrochemical impedance characteristics of the LFP module. The slower dynamics, represented by the larger time constant τ_1, correspond to the mass transport and diffusion processes through the solid electrolyte interphase (SEI) layer, whereas the faster dynamics, represented by τ_2, reflect the rapid charge transfer kinetics and double-layer effects [7]. In addition, the optimized hysteresis magnitude M_0 is estimated to be 0.0956 V, which is comparable to the maximum potential gap between the charging and discharging OCV curves at equilibrium. This corroborates the strong phase-transition characteristics inherent in LFP cathodes [64]. Concurrently, the hysteresis factor H_0 estimated at 0.0063 governs the dynamic transition rate of the hysteresis potential, which helps ensure that the proposed framework accurately tracks the transient potential lag observed during the current reversal of the DST profile [65]. Thus, this physical consistency confirms that BO successfully identifies parameters within a reasonable boundary, accurately reflecting the intrinsic electrochemical characteristics of the LFP module.

The hyperparameters α, β, κ, Q_*, and R_* of the dual-UKF were estimated via BO to validate the convergence performance of the proposed method. These parameters govern the generation of sigma points, directly influencing the estimation performance. The spread parameter α, which determines the spread of the sigma points in the UT, is optimized to a small value of 0.1; this is the quantitative evidence for the high fidelity of the EECM. This small value of α suggests that deterministic state transitions predicted by the EECM are sufficiently accurate, requiring only minimal exploration to estimate the state of the system [64]. Scaling parameter κ and distribution information β are optimized to 4 and 9, respectively. The optimized value κ of 4 confirms that the proposed method guarantees the positive semi-definiteness of the covariance matrix P_k [64]. The optimized value of β is 9, which is higher than the standard Gaussian distribution $\beta = 2$. This result suggests that the electrochemical dynamics of the LFP module exhibit severe nonlinearities that cannot be fully captured using a standard Gaussian distribution [66]. Therefore, the proposed method explicitly minimizes the higher-order approximation errors in the Taylor series expansion by adopting a large β, which helps to enhance the estimation robustness for the LFP module. In addition, the Q_* and R_* are optimized to 1×10^{-5} and 1×10^{-3}, respectively. Q_* is orders of magnitude smaller than R_*, which indicates that the proposed method has a significantly higher confidence in the SOC estimation performed by the EECM because these covariance values determine the Kalman gain, balancing the reliance on the physical model versus sensor measurements [66]. This quantitative result corroborates previous observations of α, confirming that the identified model parameters exhibit high fidelity with minimal systemic uncertainty. Hence, the optimized hyperparameters are expected to aid the dual-UKF to minimize the sensor noise and transient potential fluctuations effectively. Thus, the accurate identification of the EECM and filter parameters ensures the accurate and robust performance of the proposed method for SOC estimation.

4.2 | SOC Estimation Under Diverse Dynamic Operating Conditions

The accuracy and robustness of both the potential and SOC estimations obtained using the proposed method were evaluated

ijer, 2026, 1, Downloaded from https://onlinelibrary.wiley.com/doi/10.1155/er/7965949 by Hanyang University Library, Wiley Online Library on [01/11/2026]. See the Terms and Conditions (https://onlinelibrary.wiley.com/terms-and-conditions) on Wiley Online Library for rules of use; OA articles are governed by the applicable Creative Commons License

under diverse dynamic operating conditions. The performances were validated against initial SOC errors under three standard driving schedules: DST, FUDS, and US06 at 25°C. This validation was essential because a robust SOC estimator must autonomously compensate for initialization errors that converge to the true reference SOC. A low initial error of 5% and a severe initial error of 10% were intentionally introduced to assess the convergence capability of the proposed framework for SOC estimation against initial SOC uncertainty.

The LFP battery exhibited a self-discharge rate of ~3% per month [66]. The self-discharge can be attributed to internal chemical leakage inherent in the side reactions of the electrochemical components and the standby power consumption of the BMS during storage or idle periods [67]. Therefore, the 5% initial error reasonably reflects a real operational condition, where the LFP module has been stored for one to 2 months, resulting in a discrepancy between the recorded and actual SOC. The 10% initial error scenario represents more severe conditions resulting from both long-term storage and sensor failure. The initial SOC estimate was set to 100% in the first numerical step for all cases, while the actual experiments started at 95% and 90% SOC to represent the 5% and 10% initial error scenarios, respectively.

Figure 8 shows that the proposed method successfully estimates the SOC for all cases by rapidly compensating for the estimation

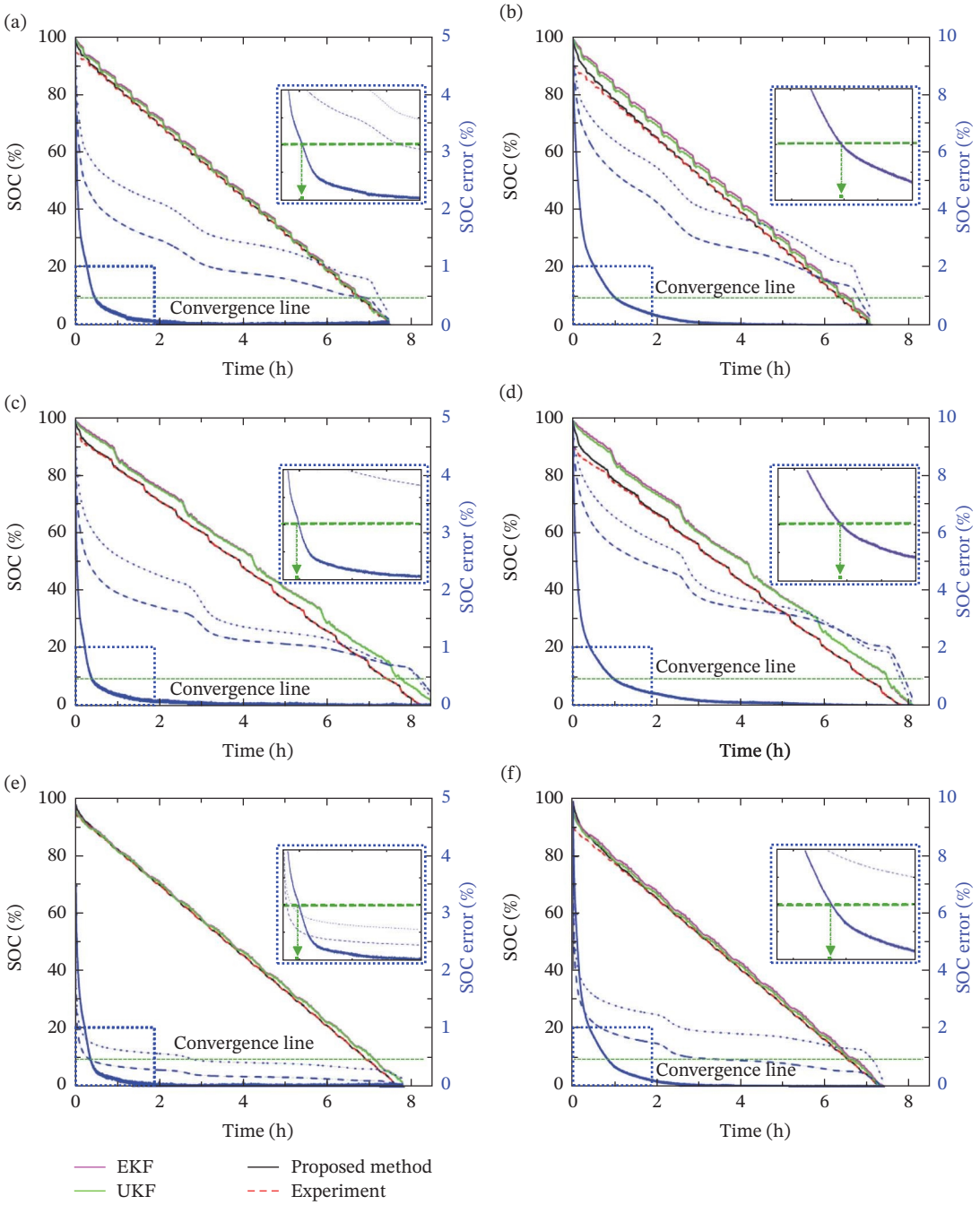

FIGURE 8 | SOC estimation results and errors under dynamic driving cycles with different initial SOC errors: (a) DST, (c) FUDS, (e) US06 cycle with 5% initial error. (b) DST, (d) FUDS, (f) US06 cycle with 10% initial error.

ijer, 2026, 1, Downloaded from https://onlinelibrary.wiley.com/doi/10.1155/er/7965949 by Hanyang University Library, Wiley Online Library on [01/11/2026]. See the Terms and Conditions (https://onlinelibrary.wiley.com/terms-and-conditions) on Wiley Online Library for rules of use; OA articles are governed by the applicable Creative Commons License

error after the start of the operation. The inset figures provide a magnified view of the initial transient phase from 0 to 2 h, effectively illustrating how the SOC estimation error decays rapidly within the designated convergence threshold. The proposed method successfully compensated for the initialization errors by rapidly driving the estimation error within a 1% convergence threshold. This rapid convergence can be attributed to the inherent characteristics of the dual-UKF, which iteratively corrects the estimated state based on the covariance of the measurement residuals [64]. The 1% error threshold (|SOC error|≤1%) is established as the primary benchmark because this threshold is widely considered a critical value for ensuring the safety of LIB modules in practical BMS applications [68]. A detailed quantitative analysis was conducted based on this threshold for an in-depth discussion of the accuracy and robustness of the proposed method.

The proposed method rapidly compensates for the initialization errors, as indicated by the convergence times listed in Table 3. In the dual-UKF, the SOC correction is governed by the terminal-potential innovation and the Kalman gain, which depends on the cross-covariance between the predicted states and terminal potential and on the innovation covariance [48]. Therefore, rapid convergence requires the measured terminal potential to contain sufficient information to distinguish an SOC mismatch from the hysteresis and polarization responses represented by the EECM. This condition is particularly important for LFP batteries because their flat pseudo-OCV characteristics inherently limit the SOC observability under weakly excited operating conditions.

The convergence times required to reach the 1% error threshold were 16.8, 15.0, and 14.8 min for the SOC estimations of the DST, FUDS, and US06 cycles, respectively, in the 5% initial error cases. This distinct trend provides critical insight into the relationship between load dynamics and estimator performances (Figure 8a,c,e). Similarly, the convergence times for the 10% initial error cases increased to 57.1, 53.8, and 46.2 min for the corresponding cycles (Table 3). This increase occurred because the larger initial deviation required more recursive measurement updates before the SOC error decreased below the 1% threshold. The substantial increase in convergence time can be attributed to the larger initial deviation in the initial error of 10% cases, as the dual-UKF requires a longer transient period to iteratively minimize the error covariance (Figure 8b,d,f).

Interestingly, the convergence times are intrinsically linked to the dynamic characteristics of each driving profile regardless of the initial error, and they followed the order US06 < FUDS < DST. Specifically, the US06 cycle resulted in the fastest convergence, while the DST cycle resulted in the slowest. US06, which is distinguished by aggressive driving behavior characterized by both high C-rates and rapid load fluctuations, provides richer excitation signals that enhance the observability of the system, resulting in faster convergence compared with the simpler patterns of the DST cycle, which is less dynamic [68]. The rapid current variations excite the Ohmic, polarization, and hysteresis dynamics of the EECM and consequently generate distinguishable terminal-potential responses. These information-rich responses increase the state–output sensitivity and enable the dual-UKF to map the terminal-potential innovation more effectively to the SOC correction. Similarly, the FUDS cycle, representing urban stop-and-go driving, showed intermediate performance, reflecting its moderately dynamic nature compared to that of US06. These results quantitatively support the theoretical relationship among dynamic excitation, system observability, and the convergence performance of the proposed dual-UKF.

The SOC RMSE values listed in Table 3 indicate that the proposed method accurately estimates the SOC with high robustness. The average SOC RMSE of 0.306% in the 5% initial error cases indicates that the proposed method ensures reliable estimation performance regardless of the complexity of the driving patterns. In the 10% initial error scenario, the proposed method successfully maintained an average SOC RMSE below the 1% threshold (0.923%), even though the extended initial transient phase contributed to a higher overall error compared with that in the 5% cases; this result demonstrates the fault tolerance capability of the proposed method. Interestingly, a similar trend was observed in terms of estimation accuracy, where the SOC RMSE followed the order US06 < FUDS < DST, which was consistent with the observed convergence speeds. This tendency in both convergence time and SOC RMSE was intrinsically linked to the dynamic characteristics of each driving profile, regardless of the magnitude of the initial error. Thus, these results confirm that rich dynamic excitation and potential fluctuations provide improved observability for SOC estimation, enabling the dual-UKF to effectively compensate for the estimation errors [69].

An additional comparison was conducted to clarify the relative contribution of each component of the proposed framework. The fixed-parameter EKF, fixed-parameter UKF, and proposed BO-based dual-UKF were evaluated using the same EECM structure, experimental datasets, initial SOC errors, sampling interval, 1% convergence threshold, and evaluation metrics. Therefore, the differences in estimation performance can be attributed primarily

TABLE 3 | Comparison of the SOC estimation accuracies for the DST, FUDS, and US06 cycles.

Initial error (%)	Quantitative value	DST	FUDS	US06	Average
5	Converge time (min)	16.8	15.0	14.8	15.5
	SOC RMSE (%)	0.32	0.31	0.29	0.306
	Potential RMSE (V)	0.054	0.078	0.074	0.068
10	Converge time (min)	57.1	53.8	46.2	52.4
	SOC RMSE (%)	0.94	0.98	0.85	0.923
	Potential RMSE (V)	0.057	0.083	0.078	0.73

ijer, 2026, 1, Downloaded from https://onlinelibrary.wiley.com/doi/10.1155/er/7965949 by Hanyang University Library, Wiley Online Library on [01/11/2026]. See the Terms and Conditions (https://onlinelibrary.wiley.com/terms-and-conditions) on Wiley Online Library for rules of use; OA articles are governed by the applicable Creative Commons License

to the state propagation and parameter adaptation strategies rather than to differences in the battery model or test conditions.

The comparison between demonstrates that the proposed method provides both faster convergence and higher SOC estimation accuracy (Tables 3 and 4). Under the 5% initial SOC error, the proposed method achieved an average convergence time of 15.5 min, compared with 352.2 min for the EKF and 252.5 min for the UKF. The corresponding average SOC RMSE values were 0.306%, 1.24%, and 0.96%, respectively. Under the more severe 10% initial error, the proposed method achieved an average convergence time of 52.4 min and an SOC RMSE of 0.923%. In contrast, the EKF required 446.1 min and produced an SOC RMSE of 3.89%, whereas the UKF required 378.6 min and produced an SOC RMSE of 2.97%. Thus, the proposed method reduced the average SOC RMSE under the 10% initial error condition by 76.3% and 68.9% relative to the EKF and UKF, respectively.

The difference among the estimators originates from their nonlinear propagation and parameter update strategies. The EKF relies on first-order Jacobian linearization and is therefore susceptible to linearization errors arising from the flat pseudo-OCV, hysteresis, and nonlinear polarization characteristics of the LFP module. The UKF reduces these errors by propagating deterministic sigma points through the nonlinear EECM; however, its fixed model parameters cannot fully compensate for changes in the electrochemical dynamics during operation. In contrast, the proposed dual-UKF first updates the EECM parameters from the terminal potential innovation and subsequently estimates the SOC using the updated model. This sequential parameter–state estimation structure maintains model consistency and enables the terminal-potential residual to be mapped more effectively to the SOC correction. Consequently, the proposed method exhibits faster convergence and greater robustness to initial SOC uncertainty than the conventional EKF and UKF.

The proposed method demonstrated high fidelity in terminal potential tracking across all tested dynamic profiles, maintaining high accuracy regardless of the magnitude of the initial errors (Figure 9). Figure 9a,c,e shows the results for the 5% initial error cases, whereas Figure 9b,d,f shows the results for the severe 10% initial error cases. The inset figures provide a magnified view of the initial transient phase from 0 to 2 h. The proposed method accurately estimates the potential using the dual-UKF framework by incorporating the EECM. The high-precision tracking of the potential profile was achieved because the model parameters of the EECM optimized via BO effectively accounted for the nonlinear electrochemical dynamics of the LFP module, including the Ohmic resistance and polarization effects [35]. As indicated in Table 3, the average potential RMSE in the 5% initial error cases across all three cycles was ~0.068 V. This was also observed under the 10% initial error condition, where the average potential RMSE was 0.073 V. A distinct trend was observed in the potential estimation compared to that of the SOC estimation results. The US06 and FUDS cycles exhibited a relatively higher potential error than the stable DST cycle; however, the US06 cycle yielded the lowest SOC error because of its enhanced observability. This phenomenon is attributed to the aggressive nature of the US06 profile, wherein rapid charge–discharge current pulses induce abrupt potential transients governed by complex polarization effects. The FUDS cycle resulted in potential errors comparable to those of the US06 cycle because its frequent stop-and-go patterns introduced continuous dynamic load fluctuations. The average potential error increasing by less than 5 mV confirms the robustness of the proposed method, despite the initial SOC deviation doubling from 5% to 10% [70]. This systematic analysis suggests that the physical parameters derived in Section 4.1 are sufficiently accurate to consider the nonlinear potential responses under varying dynamic loads with initial uncertainties. In addition, this analysis confirms that the proposed method ensures stable and accurate potential estimation against both dynamic load variations and significant initialization uncertainties.

4.3 | SOC Estimation Under Various Temperature

The SOC estimation performance of the proposed framework was evaluated under various temperature conditions by focusing on its adaptability to severe electrochemical changes. The estimation performance was evaluated under DST, FUDS, and US06 driving cycles at 45 and −15°C to validate the thermal adaptability of the proposed method. A severe initial error of 10% was intentionally introduced in all scenarios to rigorously test the convergence capability of the dual-UKF against the combined uncertainties of initialization and temperature-dependent dynamics, following the procedure outlined in Section 4.2. This validation is indispensable because ambient temperature can significantly affect the electrochemical properties of the LFP module, including the internal resistance and ion diffusion rates [71].

TABLE 4 | Comparison of the SOC estimation accuracies between EKF and UKF for the DST, FUDS, and US06 cycles.

Method	Initial error (%)	Quantitative value	DST	FUDS	US06	Average
EKF	5	Converge time (min)	378.3	495.6	182.6	352.2
		SOC RMSE (%)	1.52	1.67	0.52	1.24
	10	Converge time (min)	418.6	495.6	423.9	446.1
		SOC RMSE (%)	4.37	4.59	2.71	3.89
UKF	5	Converge time (min)	255.6	482.3	19.5	252.46
		SOC RMSE (%)	1.03	1.43	0.43	0.96
	10	Converge time (min)	409.5	473.1	253.2	378.6
		SOC RMSE (%)	3.29	4.21	1.41	2.97

ijer, 2026, 1, Downloaded from https://onlinelibrary.wiley.com/doi/10.1155/er/7965949 by Hanyang University Library, Wiley Online Library on [01/11/2026]. See the Terms and Conditions (https://onlinelibrary.wiley.com/terms-and-conditions) on Wiley Online Library for rules of use; OA articles are governed by the applicable Creative Commons License

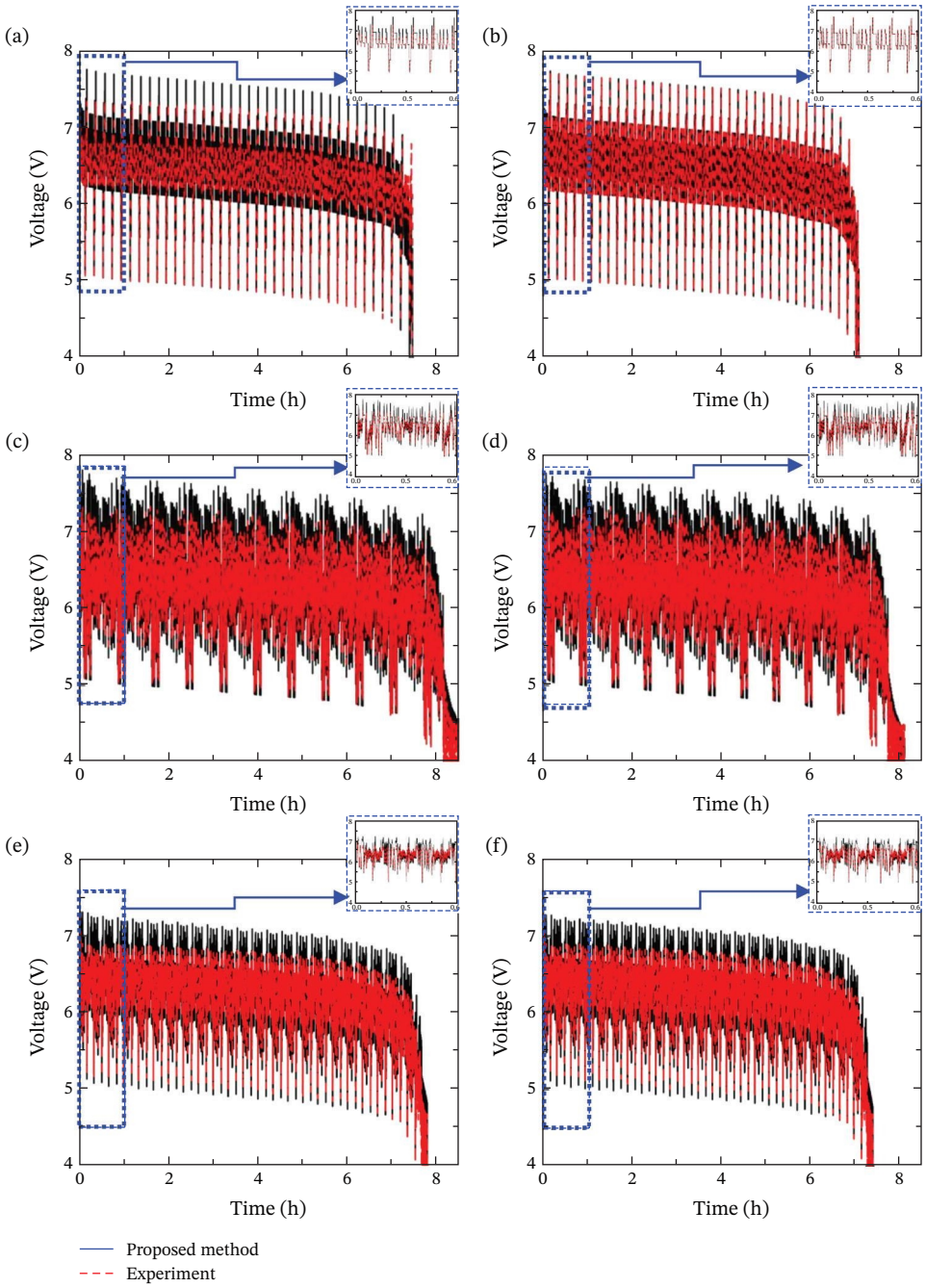

FIGURE 9 | Potential estimation results and corresponding magnified views for DST with (a) 5% and (b) 10% initial SOC errors; FUDS with (c) 5% and (d) 10% initial SOC errors; and US06 with (e) 5% and (f) 10% initial SOC errors. The insets magnify the time intervals indicated in the corresponding full-range plots.

Ambient temperature does not directly alter the electrochemical charge balance for an identical amount of the transferred charge. Instead, it affects the usable capacity and the relationship among SOC, terminal potential, and applied current by changing ionic conductivity, solid-state diffusion, charge–transfer resistance, and polarization. At room temperature, the ionic transport and charge–transfer processes remain relatively balanced, allowing the battery to deliver a capacity close to its nominal value. At high temperatures, reduced electrolyte viscosity and enhanced electrochemical kinetics increase ionic conductivity, decreasing charge–transfer resistance. These changes reduce the overpotential and allow a greater fraction of the stored charge to remain accessible during short-term operation. Consequently, the SOC decreases relatively gradually under a given load. However, prolonged high-temperature operation can accelerate side reactions and battery degradation, which were not considered in the present short-term temperature experiments [71].

In contrast, low temperatures substantially restrict lithium-ion transport. Increased electrolyte viscosity reduces ionic conductivity, while sluggish solid-state diffusion and charge–transfer kinetics increase internal resistance and polarization. The resulting overpotential causes a larger terminal-potential drop under the same applied current. Therefore, the terminal potential reaches

ijer, 2026, 1, Downloaded from https://onlinelibrary.wiley.com/doi/10.1155/er/7965949 by Hanyang University Library, Wiley Online Library on [01/11/2026]. See the Terms and Conditions (https://onlinelibrary.wiley.com/terms-and-conditions) on Wiley Online Library for rules of use; OA articles are governed by the applicable Creative Commons License

the discharge cut-off earlier, reducing the usable capacity and producing a more rapid decrease in the experimentally available SOC. This rapid SOC decrease does not indicate that the temperature directly consumes the stored charge. Rather, it originates from the reduced accessibility of the stored capacity and the increased potential loss caused by transport limitations at low temperatures [72].

This physical interpretation is supported by the experimental results in Figures 10–12. The experimental SOC trajectory decreased more rapidly at −15°C than at 45°C, indicating that the low-temperature module reached its usable discharge limit earlier. Furthermore, the potential variations for the DST, FUDS, and US06 cycles increased from 0.033, 0.048, and 0.025 V at 45°C to 0.062, 0.086, and 0.050 V at −15°C, respectively. These ~1.8–2.0-fold increases confirm that limited lithium transport and increased overpotential intensify the terminal-potential response at low temperatures. The temperature-dependent pseudo-OCV look-up table and recursively updated EECM parameters compensate for these variations, enabling the proposed framework to maintain an average SOC RMSE below 1% across the tested temperature range.

As shown in Figure 10, the proposed method successfully estimates the SOC at 45 and −15°C by compensating for the initial 10% error rapidly after the operation begins. The estimated SOC from the proposed method aligns well with the reference SOC.

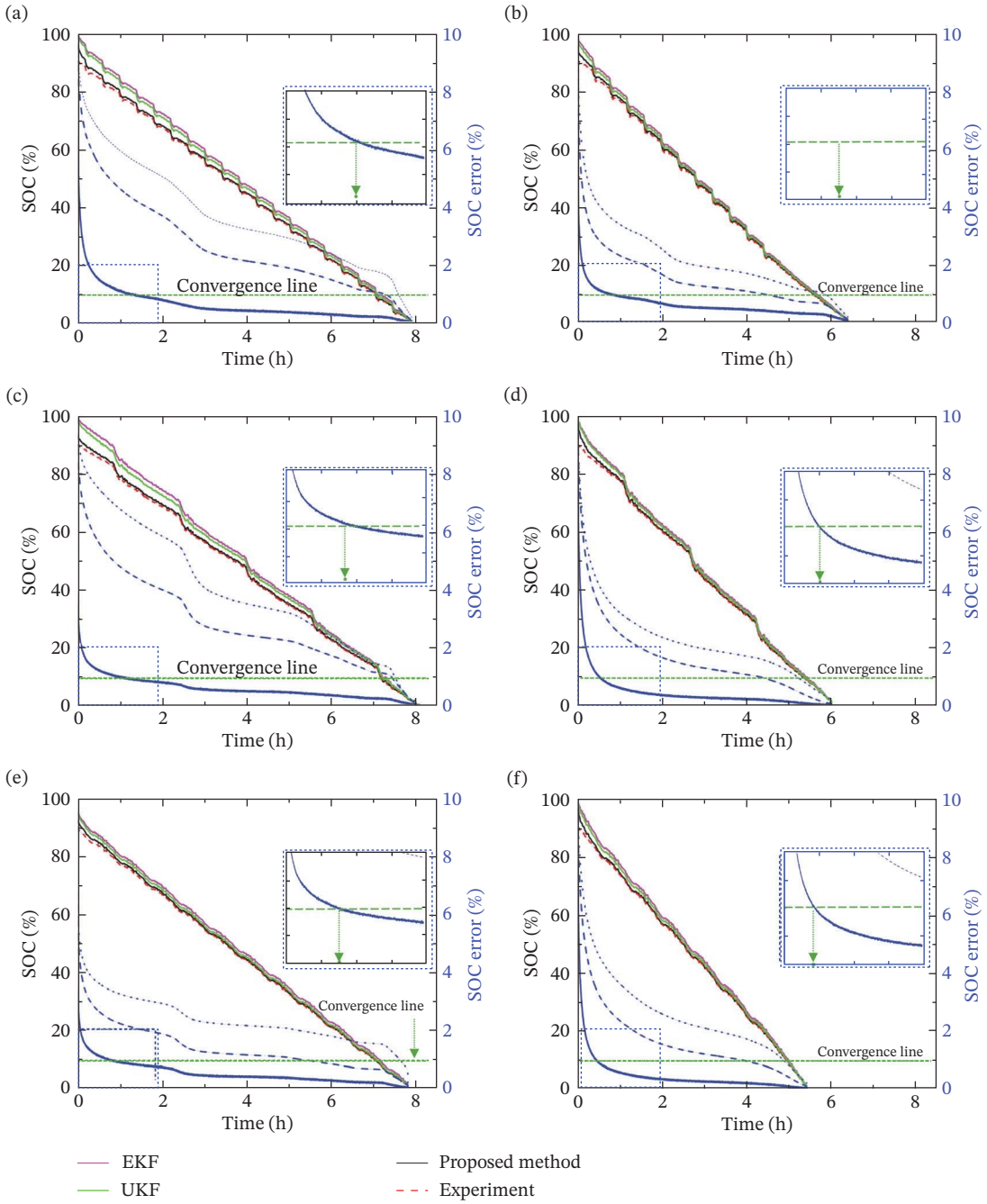

FIGURE 10 | SOC estimation results and errors under dynamic driving cycles with a 10% initial SOC error: (a) DST, (c) FUDS, and (e) US06 cycles at 45°C. (b) DST, (d) FUDS, and (f) US06 cycles at −15°C.

ijer, 2026, 1, Downloaded from https://onlinelibrary.wiley.com/doi/10.1155/er/7965949 by Hanyang University Library, Wiley Online Library on [01/11/2026]. See the Terms and Conditions (https://onlinelibrary.wiley.com/terms-and-conditions) on Wiley Online Library for rules of use; OA articles are governed by the applicable Creative Commons License

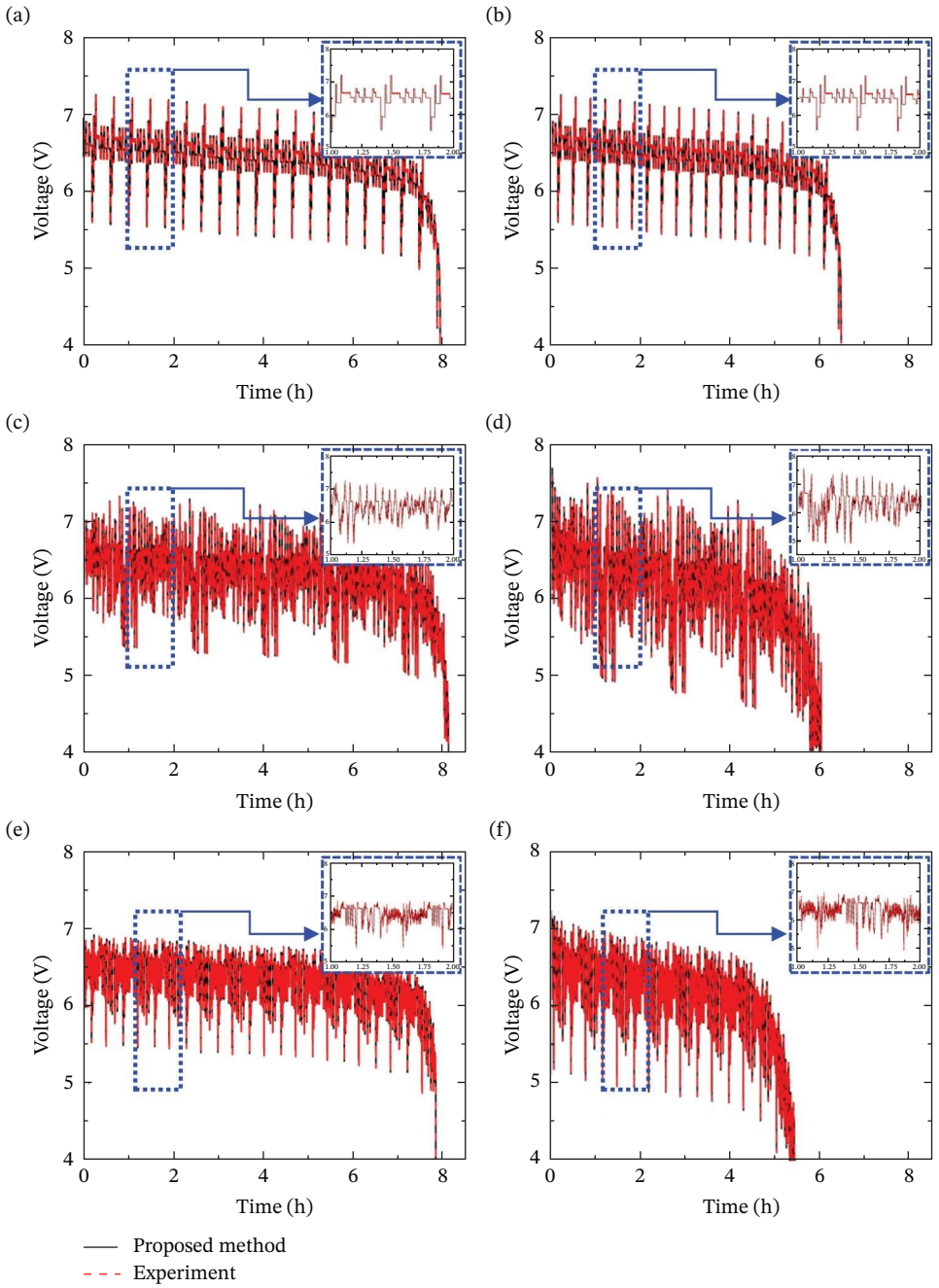

FIGURE 11 | Potential profile under dynamic driving cycles with a 10% initial SOC error: (a) DST, (c) FUDS, and (e) US06 cycles at 45°C. (b) DST, (d) FUDS, and (f) US06 cycles at −15°C.

Figure 10a,c,e shows the results for the 10% initial error case cycles at 45°C, whereas Figure 10b,d,f shows the results for the severe 10% initial error case cycles at −15°C. The inset figures provide a magnified view of the initial transient phase from 0 to 2 h, effectively illustrating how the SOC estimation error decays rapidly within the designated convergence threshold. The proposed method compensates for initialization errors across all scenarios within the 1% benchmark threshold. However, the convergence characteristics exhibit distinct trends based on the operating temperature. Thus, a detailed quantitative analysis is conducted to discuss the relationship between the temperature-dependent electrochemical characteristics and the estimator performance.

The convergence times listed in Table 5 reveal a significant temperature-dependent trend. The convergence times required to reach a 1% error threshold were 63.3, 55.9, and 48.1 min for the SOC estimation of the DST, FUDS, and US06 cycles at 45°C in the 10% initial error cases. In contrast, the estimator exhibited faster error correction capabilities under the low-temperature condition; the convergence times required to reach a 1% error threshold were 46.2, 30.9, and 27.4 min for the SOC estimation of the DST, FUDS, and US06 cycles at −15°C in the 10% initial error cases. The average convergence time required to reach a 1% error threshold was ~34.8 min at −15°C, which was significantly faster than the 55.8 min recorded at 45°C. The overall reduction in convergence time at −15°C compared with that at 45°C indicates

ijer, 2026, 1, Downloaded from https://onlinelibrary.wiley.com/doi/10.1155/er/7965949 by Hanyang University Library, Wiley Online Library on [01/11/2026]. See the Terms and Conditions (https://onlinelibrary.wiley.com/terms-and-conditions) on Wiley Online Library for rules of use; OA articles are governed by the applicable Creative Commons License

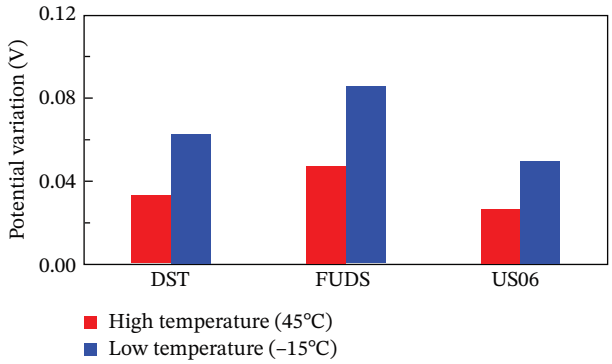

FIGURE 12 | Potential variation under dynamic driving cycles with a 10% initial SOC error.

that the intensified potential dynamics induced by low-temperature polarization provide richer excitation signals [72]. This enhances the observability of the dual-UKF. Furthermore, the convergence times were intrinsically linked to the dynamic characteristics of each driving profile, regardless of the operating temperature, consistently following the order US06 < FUDS < DST.

The comparison further demonstrates the advantage of the proposed method under temperature-dependent model uncertainty (Tables 5 and 6). At 45°C, the proposed method achieved an average convergence time of 55.8 min and an SOC RMSE of 0.93%, whereas the corresponding values were 471.3 min and 3.36% for the EKF and 422.4 min and 2.49% for the UKF, respectively. At −15°C, the proposed method achieved an average convergence time of 34.8 min and an SOC RMSE of 0.88%, compared with 343.2 min and 2.36% for the EKF and 275.8 min and 1.85% for the UKF. Therefore, the proposed method maintained an average SOC RMSE below 1% at both temperatures, while the fixed-parameter EKF and UKF exceeded this threshold. These results confirm that nonlinear sigma-point propagation alone improves SOC estimation compared with Jacobian-based linearization, while the recursive parameter adaptation of the dual-UKF provides an additional improvement by compensating for temperature-dependent changes in resistance, polarization, and hysteresis.

The SOC RMSE listed in Table 5 ensures that the proposed method accurately estimates the SOC with high robustness, regardless of ambient temperature. The RMSEs are 0.98%, 0.95%, and 0.87% for the DST, FUDS, and US06 cycles at 45°C, respectively. The average SOC RMSE of 0.93% at 45°C confirms that the proposed method ensures reliable SOC estimation performance even under high-temperature conditions. The RMSEs are 0.87%, 0.94%, and 0.83% for the DST, FUDS, and US06 at −15°C, which results in an average RMSE of 0.88% at −15°C. The proposed method successfully maintains an average SOC RMSE below the 1% threshold under all temperature conditions, although the severe initial error of 10% is applied. The average RMSE remained below the 1% target even at −15°C, which demonstrates the fault tolerance capability of the proposed method against severe electrochemical nonlinearity. A similar trend in convergence times is observed in the estimation accuracy, where the SOC RMSE followed the order US06 < FUDS < DST, implying that the dynamic characteristics of each driving

TABLE 5 | Comparison of SOC estimation accuracy for the DST, FUDS, and US06 cycles under different temperatures.

Initial error (%)	Temperature (°C)	Quantitative value	DST	FUDS	US06	Average
10	45	Converge time (min)	63.3	55.9	48.1	55.8
		SOC RMSE (%)	0.98	0.95	0.87	0.093
		Potential RMSE (V)	0.061	0.087	0.082	0.077
	−15	Converge time (min)	46.1	30.9	27.4	34.8
		SOC RMSE (%)	0.87	0.94	0.83	0.88
		Potential RMSE (V)	0.051	0.079	0.072	0.67

TABLE 6 | Comparison of SOC estimation accuracy between EKF and UKF under DST, FUDS, and US06 driving cycles across various temperatures with a 10% initial estimation error.

Methods	Temperature (°C)	Quantitative value	DST	FUDS	US06	Average
EKF	45	Converge time (min)	471.8	468.6	473.5	471.3
		SOC RMSE (%)	3.77	4.12	2.19	3.36
	−15	Converge time (min)	334.6	342.9	352.1	343.2
		SOC RMSE (%)	2.24	2.11	2.74	2.36
UKF	45	Converge time (min)	452.2	457.9	357.2	422.4
		SOC RMSE (%)	2.92	3.05	1.52	2.49
	−15	Converge time (min)	283.3	285.9	258.2	275.8
		SOC RMSE (%)	1.73	1.82	2.01	1.85

ijer, 2026, 1, Downloaded from https://onlinelibrary.wiley.com/doi/10.1155/er/7965949 by Hanyang University Library, Wiley Online Library on [01/11/2026]. See the Terms and Conditions (https://onlinelibrary.wiley.com/terms-and-conditions) on Wiley Online Library for rules of use; OA articles are governed by the applicable Creative Commons License

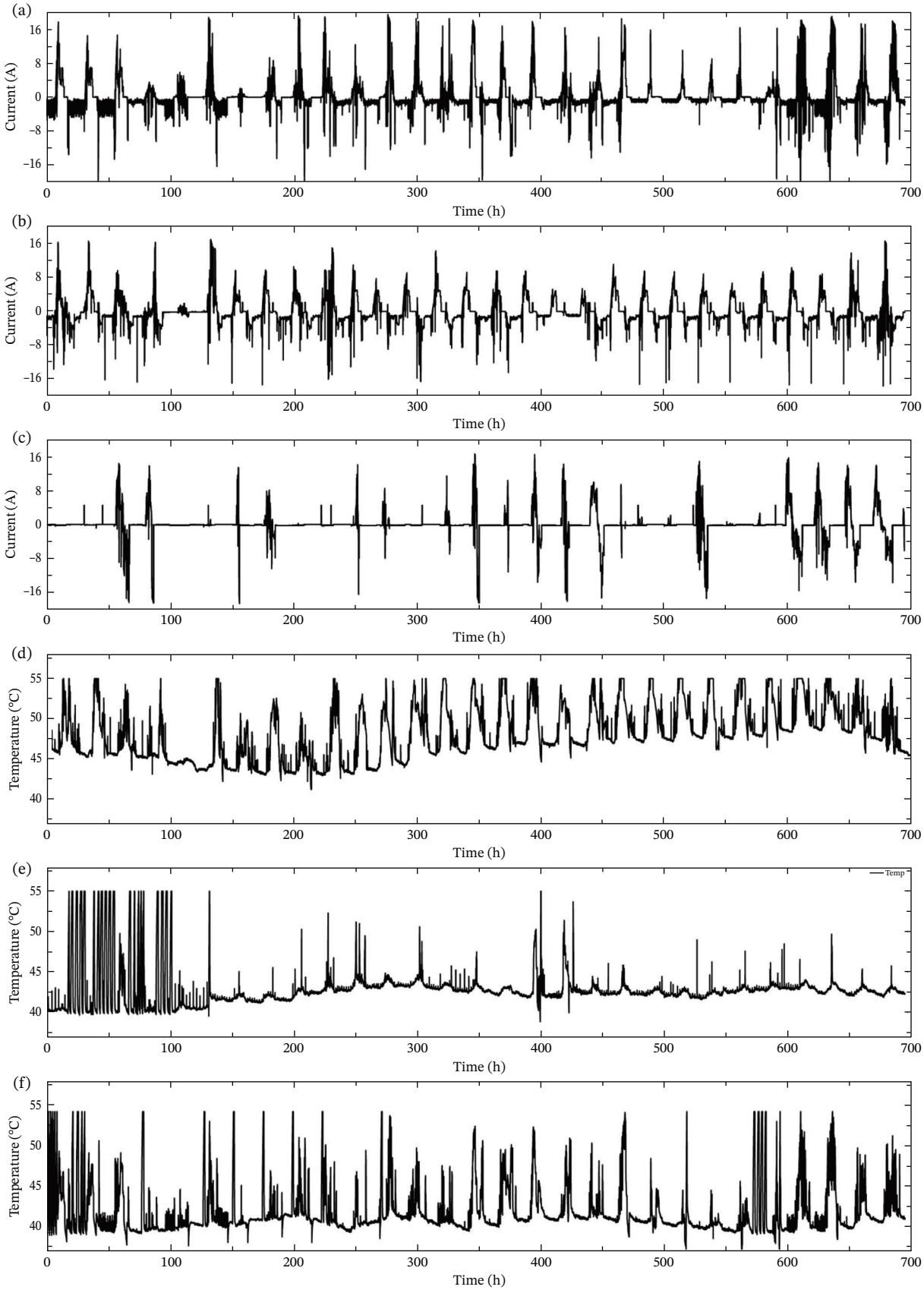

FIGURE 13 | Current profiles of the BESS operating conditions at the European site during (a) March, (b) August, and (c) December, and the corresponding temperature profiles during (d) March, (e) August, and (f) December.

ijer, 2026, 1, Downloaded from https://onlinelibrary.wiley.com/doi/10.1155/er/7983949 by Hanyang University Library, Wiley Online Library on [01/11/2026]. See the Terms and Conditions (https://onlinelibrary.wiley.com/terms-and-conditions) on Wiley Online Library for rules of use; OA articles are governed by the applicable Creative Commons License

TABLE 7 | Characteristics for the BESS under stochastic operational conditions.

Quantitative value	March	August	December	Average
Average temperature (°C)	44.7	47.9	42.0	44.9
Cumulative capacity (kAh)	567.7	595.2	271.8	478.2

profile affect the estimator performance regardless of temperature. These results confirm that rich dynamic excitation provides improved observability for SOC estimation, enabling the dual-UKF to effectively compensate for estimation errors.

Figure 11 shows the high fidelity and accuracy of terminal potential tracking across all tested dynamic profiles, regardless of operating temperature. The inset figure provides a magnified view from 1 to 2 h, revealing that the proposed method provides an accurate estimation of the potential profile. Figure 11a,c,e shows the results for the 10% initial error case cycles at 45°C, whereas Figure 11b,d,f shows the results for the severe 10% initial error case cycles at −15°C. These results can be attributed to the model parameters of the EECM optimized via BO effectively accounting for the temperature-dependent nonlinear electrochemical dynamics of the LFP module, including the Ohmic resistance and polarization effects. A distinct trend was observed in the potential estimation (Table 4), which was similar to that of the SOC estimation results. The US06 and FUDS cycles exhibited relatively higher potential errors than the stable DST cycle owing to their rapid load fluctuations. In addition, the potential variation at −15°C was significantly larger than that at 45°C because of increased polarization [73]. The US06 cycle at −15°C yielded the lowest SOC error because of the enhanced observability derived from this potential variation. Thus, the average potential error remained below 0.1 V even under the severe −15°C condition, confirming the robustness of the proposed method against extreme environmental variations.

Interestingly, the proposed method ensured a more accurate SOC estimation performance under low-temperature conditions than under high-temperature conditions. The low-temperature operation induces a large overpotential effect because the sluggish electrochemical reactions provide rich excitation signals for the dual-UKF. The intensified overpotential fluctuations at low temperatures inject more information into the dual-UKF, enhancing the observability of correcting the initial offset more aggressively [72]. This phenomenon can be attributed to the electrochemical characteristics of lithium ions at different temperatures. The viscosity of the electrolyte increases, and the diffusion rate of lithium ions within the solid active material decreases significantly at low temperatures, resulting in a substantial increase in internal impedance and significant overpotential effects [72]. In contrast, the high temperature enhances the electrochemical kinetics of the LIB, resulting in both increased ionic conductivity of the electrolyte and reduced charge-transfer resistance at the electrode–electrolyte interface during the intercalation/de-intercalation processes [71]. Therefore, distinguishing the dynamic potential response from steady-state characteristics is essential for quantitatively verifying this mechanism. This study isolates pure dynamic overpotential components from static thermodynamic potential using the potential variation ϕ_k. This is calculated by subtracting the OCV from the measured potential as

$$\phi_k = V_k + \mathrm{OCV}(\mathrm{SOC}_k), \tag{25}$$

where ϕ_k represents the potential variation at each step.

Figure 12 displays a comparison of the average potential variations for each driving cycle. The potential variation at −15°C exhibited a substantial increase compared with that at the 45°C condition. The potential variations for the DST, FUDS, and US06 cycles were 0.033, 0.048, and 0.025 V at 45°C, respectively; under the −15°C condition, these values increased significantly to 0.062, 0.086, and 0.050 V, respectively. This quantitative evidence confirms that sluggish kinetics and increased internal resistance at low temperatures induce significantly larger potential swings. Hence, these amplified dynamic variations serve as information-rich signals for the dual-UKF, enhancing the observability of the system and enabling a robust estimation performance in low-temperature scenarios.

4.4 | Application for BESS: Stochastic Operational Conditions

We evaluated the robustness of the proposed SOC estimation framework under stochastic operating conditions for BESS applications. The experimental protocols were generated from field monitoring data collected from a single module of a residential BESS (28s9p, 45 Ah) installed in Northern Europe. The nominal capacity of an individual cell within the BESS was 5 Ah. Therefore, the measured current profiles were scaled by the C-rate to compensate for the capacity difference between the reference system and the LFP module (2s4p, 60 Ah). This scaling aimed to ensure that the LFP module was subjected to the same relative current density as the actual field-deployed system for preserving the intrinsic load characteristics derived from household demand and photovoltaic (PV) generation [74]. Figure 13 shows that the protocols distinctively reflect the stochastic nature of BESS operations, which exhibit significant seasonal dependencies. As indicated in Table 7, the cumulative capacity for each month decreased from a peak of 595.2 kAh in August (summer) to 271.8 kAh in December (winter); this represents a 54.3% reduction in operational intensity due to the limited solar irradiance (Figure 13a–c). Similarly, the average temperature of the indoor BESS followed the order of December (42.0°C) < March (44.7°C) < August (47.9°C), reflecting seasonal characteristics driven by the extended daylight hours and high solar altitude typical of Northern European summer (Figure 13d,f,g) [75]. Thus, these protocols validate actual field applications characterized by non-repeating stochastic currents coupled with varying temperatures. The severe initial error of 10% was intentionally introduced in all scenarios to rigorously test the convergence capability of the dual-UKF against the combined uncertainties of initialization and temperature-dependent dynamics.

Figure 14 presents the validation results of the proposed framework under the stochastic BESS operational profiles for March, August, and December. The estimated SOC and terminal potential accurately tracked the experiments throughout the entire 1-month operation period for all seasonal cases, with both the

ijer, 2026, 1, Downloaded from https://onlinelibrary.wiley.com/doi/10.1155/er/7965949 by Hanyang University Library, Wiley Online Library on [01/11/2026]. See the Terms and Conditions (https://onlinelibrary.wiley.com/terms-and-conditions) on Wiley Online Library for rules of use; OA articles are governed by the applicable Creative Commons License

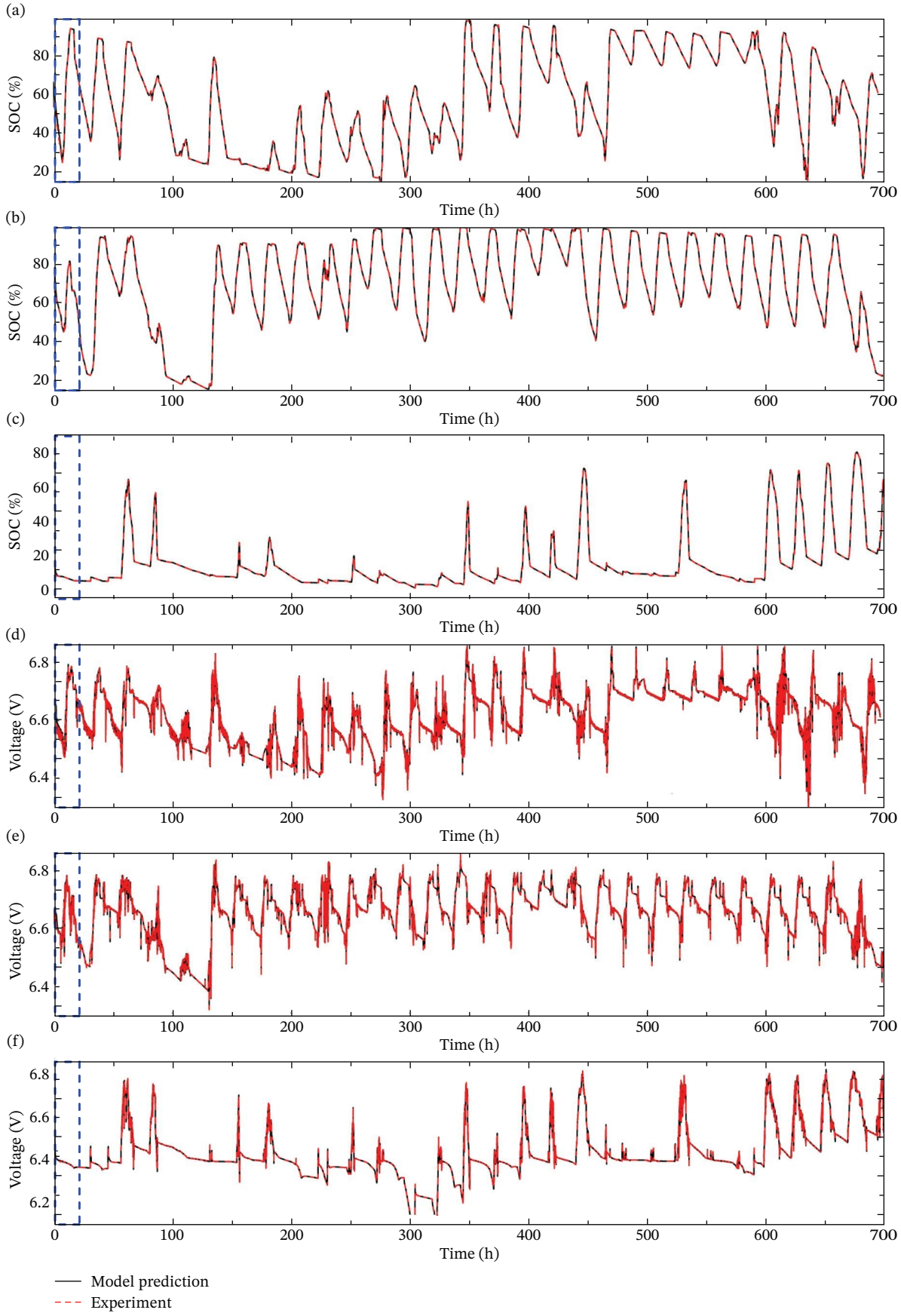

FIGURE 14 | SOC estimation for the operating condition of the BESS during (a) March, (b) August, and (c) December. The potential estimation results for the operating condition of the BESS during (d) March, (e) August, and (f) December.

ijer, 2026, 1, Downloaded from https://onlinelibrary.wiley.com/doi/10.1155/er/7965949 by Hanyang University Library, Wiley Online Library on [01/11/2026]. See the Terms and Conditions (https://onlinelibrary.wiley.com/terms-and-conditions) on Wiley Online Library for rules of use; OA articles are governed by the applicable Creative Commons License

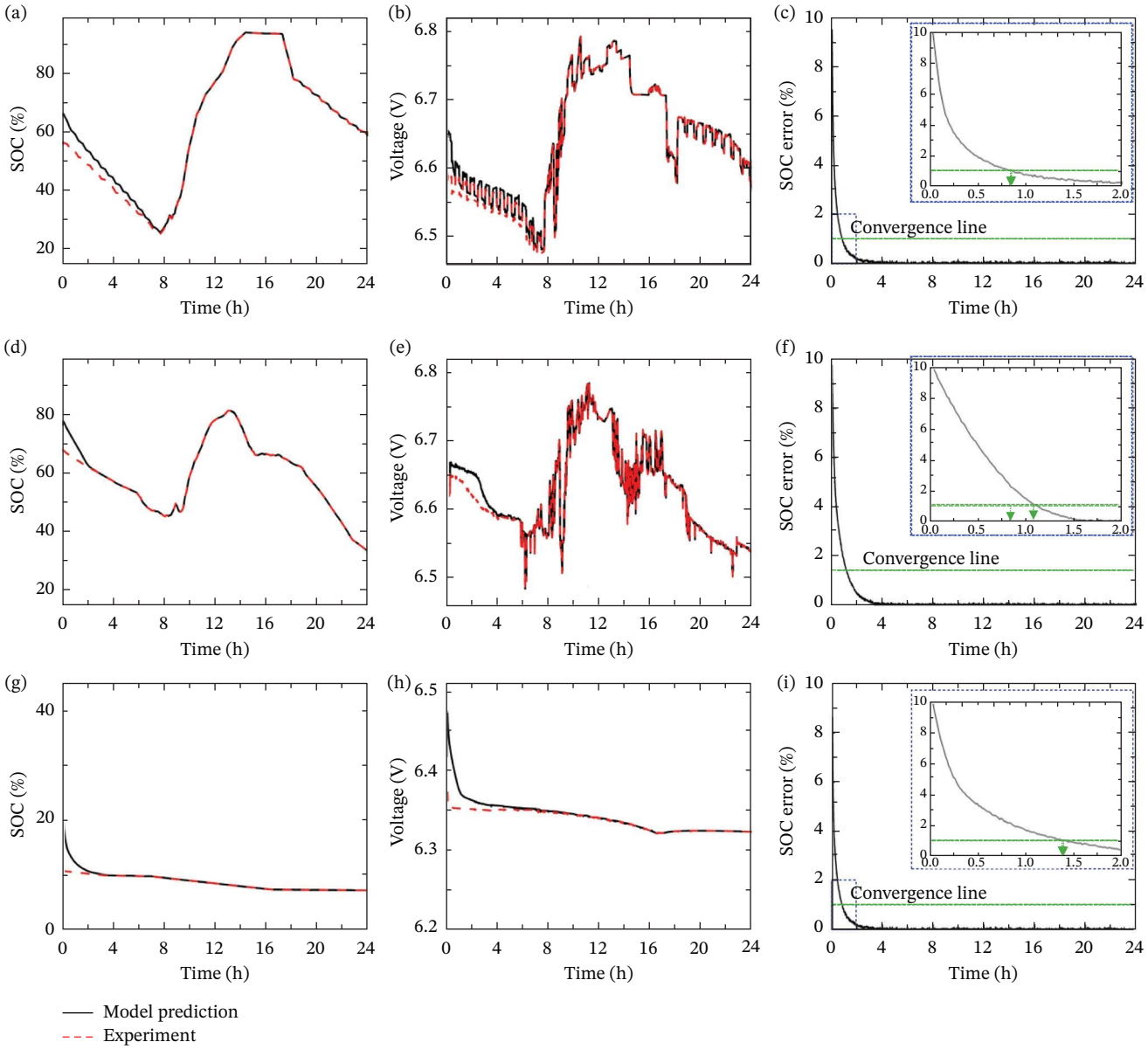

FIGURE 15 | SOC estimation for the operating condition from 24 h of the BESS during (a) March, (d) August, and (g) December. The SOC error during (b) March, (e) August, and (h) December. The potential estimation results during (c) March, (f) August, and (i) December.

severe initialization error of 10% and highly fluctuating load conditions (Figure 14a–f). The results demonstrated that the proposed dual-UKF framework accurately estimated both the SOC and the potential by effectively handling the stochasticity of residential BESS operations characterized by irregular protocols and seasonal temperature variations (Figure 15a,d,g). The estimation error, initially set at 10%, rapidly decayed and converged within the 1% error threshold (green dotted lines in the insets in Figure 15b,e,h). The quantitative analysis supports this rapid convergence capability (Table 8). The convergence times required to reach a 1% error threshold starting from the 10% initial error were 63.1 and 66.3 min for March and August, respectively. In

TABLE 8 | Comparison of SOC estimation accuracy for the stochastic operational condition.

Initial error (%)	Quantitative value	March	August	December	Average
10	Converge time (min)	63.1	66.3	84.6	71.3
	SOC RMSE (%)	0.44	0.45	0.30	0.39
	Potential RMSE (V)	0.0062	0.0046	0.0039	0.0049

ijer, 2026, 1, Downloaded from https://onlinelibrary.wiley.com/doi/10.1155/er/7965949 by Hanyang University Library, Wiley Online Library on [01/11/2026]. See the Terms and Conditions (https://onlinelibrary.wiley.com/terms-and-conditions) on Wiley Online Library for rules of use; OA articles are governed by the applicable Creative Commons License

contrast, December required a relatively long duration (84.6 min) to reach the convergence threshold. This distinct trend provides critical insight into the relationship between the richness of the excitation signals and estimation performance. The operational profiles in March and August were characterized by both higher cumulative capacities and current fluctuations, providing rich dynamic excitation that enhanced the observability. This improved observability enables the dual-UKF to rapidly correct the state covariance, thereby accelerating the convergence speed [76].

In contrast, the December profile governed by low-current standby periods attributed to limited PV generation includes less dynamic information, which results in a prolonged transient phase to compensate for the initial uncertainty [77]. The SOC RMSE values listed in Table 8 show that the proposed framework ensures high estimation accuracy once convergence is achieved. The estimation accuracy exhibited an inverse trend compared with that of the convergence speed. The December profile, which was the slowest to converge, yielded the lowest RMSE. This was attributed to the stationary nature of the winter season. This is because a relatively stable and low-current operation reduces polarization-induced nonlinearities, enabling stable tracking with the minimal steady-state error after convergence [78]. Consequently, the proposed method successfully maintains an average SOC RMSE significantly below the 1% safety threshold under all seasonal conditions, confirming its robustness against both severe initial errors and stochastic environmental factors. Finally, the proposed framework exhibits high fidelity in terminal potential tracking (insets of Figure 15c,f,i). The average potential RMSE value of 0.0049 V indicated that the optimized EECM parameters effectively captured the electrochemical response of the 2s4p LFP module, even under real-world stochastic loads. This accurate potential tracking capability confirms that the proposed method can reliably monitor the SOC and potential in practical BESS applications [79].

The present study validates the proposed framework under temperature variations, dynamic load profiles, and initial SOC uncertainty but does not establish its estimation accuracy under battery aging conditions. The proposed EECM represents the aggregate behavior of the 2s4p module through averaged pseudo-OCV characteristics and equivalent circuit parameters. Therefore, the parameter, UKF, can recursively update the equivalent resistance, capacitance, and hysteresis parameters and may compensate for moderate aging-induced changes in the overall module dynamics. However, the current framework retains a fixed nominal capacity and does not explicitly estimate capacity degradation. Future work will incorporate joint SOC–SOH and capacity estimation and validate the extended framework by using LFP modules at degradation stages with potential, capacity, resistance, and temperature measurements.

5 | Conclusion

A robust SOC estimation framework for a 2s4p LFP battery module is proposed in this study. This framework was integrated into the EECM with a dual-UKF optimized via BO. The proposed method demonstrated superior robustness against initialization errors of up to 10% under various dynamic driving cycles, rapidly converging within a 1% safety threshold. Comprehensive validation across a wide temperature range from −15 to 45°C revealed that the framework maintained high accuracy regardless of thermal variations. Quantitative analysis confirmed that the increased potential variation induced by sluggish electrochemical kinetics at −15°C enhanced observability, resulting in faster convergence compared with that under high-temperature conditions. In addition, the practical applicability of the framework was validated using real-world stochastic BESS operational data. The framework achieved an average RMSE of 0.39% despite seasonal load fluctuations. Consequently, this study confirmed that the proposed physics-based adaptive framework provides a reliable solution for accurate SOC monitoring in the LFP-based BESS, ensuring safe operation under diverse environmental and operational uncertainties. However, the proposed method requires a greater computational effort than a single EKF or UKF, and BO introduces an additional offline calibration process. The framework also requires module-specific pseudo-OCV and EECM characterization and does not explicitly estimate cell-specific capacity fade, state of health, or persistent sensor bias. Therefore, future work will focus on reducing the computational burden and extending the framework to joint SOC–SOH, capacity, and sensor bias estimation for aged and cell-imbalanced battery modules.

Nomenclature

Symbols

BESS:	Battery energy storage system
BMS:	Battery management system
BO:	Bayesian optimization
DST:	Dynamic stress test
ECM:	Equivalent circuit model
EKF:	Extended Kalman filter
EV:	Electric vehicle
FUDS:	Federal urban driving schedule
LFP:	Lithium iron phosphate
LIB:	Lithium-ion battery
OCV:	Open circuit potential
PDE:	Partial differential equation
RMSE:	Root-mean-square error
SEI:	Solid electrolyte interphase
SOC:	State of charge
UKF:	Unscented Kalman filter
US06:	United States 06 (Supplemental Federal Test Procedure)
UT:	Unscented transformation.

Author Contributions

Jun-Hyeong Kim: methodology, conceptualization, formal analysis, writing – original draft, writing – review and editing. **Eunji Kwak**: validation, investigation. **Jinho Jeong**: data curation, software. **Ki-Yong Oh:** conceptualization, formal analysis, writing – review and editing, funding acquisition, supervision, project administration.

ijer, 2026, 1, Downloaded from https://onlinelibrary.wiley.com/doi/10.1155/er/7965949 by Hanyang University Library, Wiley Online Library on [01/11/2026]. See the Terms and Conditions (https://onlinelibrary.wiley.com/terms-and-conditions) on Wiley Online Library for rules of use; OA articles are governed by the applicable Creative Commons License

Acknowledgments

This work was supported by the Fire Safety Standards Development for Transportation and Storage Stage of Reuse Battery funded by the National Fire Agency (NFA, Korea) (Grant number RS-2024-00408270), the National Research Foundation of Korea (NRF) grant funded by the Korea government (MSIT) (Grant RS-2025-00514361), and the ANCHOR through the Seoul ANCHOR Center, funded by the Ministry of Education (MOE) and the Seoul Metropolitan Government (Grant 2026-ANCHOR-01-027-04).

Funding

This work was supported by the Fire Safety Standards Development for the Transportation and Storage Stage of Reuse Battery funded by the National Fire Agency (NFA, Korea) (Grant RS-2024-00408270), the National Research Foundation of Korea (NRF) grant funded by the Korea government (MSIT) (Grant RS-2025-00514361), and the ANCHOR through the Seoul ANCHOR Center, funded by the Ministry of Education (MOE) and the Seoul Metropolitan Government (Grant 2026-ANCHOR-01-027-04).

Conflicts of Interest

The authors declare no conflicts of interest.

Data Availability Statement

Data will be made available upon request.

References

1. H. Ali, H. A. Khan, M. Khalid, and M. Pecht, "A Review and Analysis of the Safety Labeling of Lithium-Ion Batteries," *Journal of Energy Storage* 120 (2025): 116461.

2. Y. Xu, Z. Zhang, Y. Fan, J. Yao, Z. Zhao, and S. Liu, "Safety Charging Boundary Prediction of Ternary Lithium-Ion Batteries Based on the SP+ Model," *International Journal of Energy Research* 2025 (2025): 3801048.

3. M. Zheng, Y. You, and J. Lu, "Understanding Materials Failure Mechanisms for the Optimization of Lithium-Ion Battery Recycling," *Nature Reviews Materials* 10, no. 5 (2025): 355–368.

4. J.-H. Kim, E. Kwak, and K.-Y. Oh, "Degradation Pathways Dependency of a Lithium Iron Phosphate Battery on Temperature and Compressive Force," *International Journal of Energy Research* 45, no. 5 (2021): 6888–6906.

5. W. Black, S. Azam, H. MacLennan, M. Metzger, and J. R. Dahn, "Understanding Capacity Loss in LFP/Graphite Pouch Cells at High Temperatures Through Modelling," *Journal of the Electrochemical Society* 172, no. 9 (2025): 090503.

6. J.-H. Kim, E. Kwak, J. Jeong, and K.-Y. Oh, "Versatile Multiphysics Model for Thermal Runaway Estimation of a Lithium-Ion Battery," *International Journal of Energy Research* 46, no. 12 (2022): 16550–16575.

7. J.-H. Kim, E. Kwak, J. Jeong, and K.-Y. Oh, "Control-Oriented Multiphysics Model of a Lithium-Ion Battery for Thermal Runaway Estimation Under Operational and Abuse Conditions," *Applied Thermal Engineering* 254 (2024): 123895.

8. L. Sheng, C. Zhang, J. Xu, Q. Zhou, and X. Zhang, "Quantitative Measurement of Thermal Performance of a Cylindrical Lithium-Ion Battery," *Measurement* 239 (2025): 115458.

9. B. Huang, H. Li, J. Sun, et al., "Robust SOC Estimation for Lithium-Ion Batteries: Combination of GRU and FOMIAUKF Approach With an Improved State Transition Matrix," *Energy* 328 (2025): 136429.

10. W. Zhang, R. Ahmed, and S. Habibi, "State-of-Health Estimation for Lithium-Ion Batteries Based on Electrochemical Impedance Spectroscopy Measurements Combined With Unscented Kalman Filter," *Journal of Power Sources* 625 (2025): 235450.

11. F. Mohammadi, "Lithium-Ion Battery State-of-Charge Estimation Based on an Improved Coulomb-Counting Algorithm and Uncertainty Evaluation," *Journal of Energy Storage* 48 (2022): 104061.

12. C. Hu, B. Li, L. Ma, and F. Cheng, "State-of-Charge Estimation for Lithium-Ion Batteries of Electric Vehicle Based on Sensor Random Error Compensation," *Journal of Energy Storage* 55 (2022): 105537.

13. H. Zhao, C. Liao, C. Zhang, L. Wang, and L. Wang, "State-of-Charge Estimation of Lithium-Ion Battery: Joint Long Short-Term Memory Network and Adaptive Extended Kalman Filter Online Estimation Algorithm," *Journal of Power Sources* 604 (2024): 234451.

14. Y. Fan, Z. Huang, H. Li, M. B. Kaleem, R. Zhang, and W. Liu, "State of Charge Estimation for Lithium-Ion Batteries With Enhanced Open-Circuit Voltage Model," *Measurement* 251 (2025): 117124.

15. L. Wang, J. Duan, S. Fan, and K. Zhao, "An Estimated Value Compensation Method for State of Charge Estimation of Lithium Battery Based on Open Circuit Voltage Change Rate," *Energy* 313 (2024): 134119.

16. Y. Li and P. Hu, "Addressing the OCV-SOC Flat Region in LFP Cells for SOC Estimations Using EIS Measurements," *Journal of the Electrochemical Society* 173, no. 2 (2026): 020503.

17. Y. Gao and S. Onori, "Advancing SOC Estimation in LiFePO4 Batteries: Enhanced dQ/dV Curve and Short-Pulse Methods," *eTransportation* 26 (2025): 100466.

18. S. Kadiwala, P. Savsaviya, S. V. Pandey, et al., "Decoding Degradation: The Synergy of Partial Differential Equations and Advanced Predictive Models for Lithium-Ion Battery," *Journal of Power Sources* 627 (2025): 235771.

19. I. Lopetegi, G. L. Plett, M. S. Trimboli, et al., "A New Battery SOC/SOH/eSOH Estimation Method Using a PBM and Interconnected SPKFs: Part I. SOC and Internal Variable Estimation," *Journal of the Electrochemical Society* 171, no. 3 (2024): 030519.

20. J. Wang, J. Meng, Q. Peng, et al., "Lithium-Ion Battery State-of-Charge Estimation Using Electrochemical Model With Sensitive Parameters Adjustment," *Batteries* 9, no. 3 (2023): 180.

21. H. Pang, X. Yan, N. Jiang, G. Fan, J. Du, and G. Lin, "Towards Co-Estimation of Lithium-Ion Battery State of Charge and State of Temperature Using a Thermal-Coupled Extended Single-Particle Model," *Energy* 326 (2025): 136186.

22. Z. Tao, Z. Zhao, C. Wang, et al., "State of Charge Estimation of Lithium Batteries: Review for Equivalent Circuit Model Methods," *Measurement* 236 (2024): 115148.

23. X. Zhang, Y. Wang, and Z. Chen, "SoC-Modified Core Temperature Estimation of Lithium-Ion Battery Based on Control-Oriented Electro-Thermal Model," *IEEE Transactions on Power Electronics* 38, no. 9 (2023): 11642–11651.

24. J. Shen, X. Liu, C. Zhou, et al., "Accurate Co-Estimation of SOC and SOH for Lithium-Ion Batteries Across Lifespan and Wide Temperature Ranges," *IEEE Transactions on Transportation Electrification* 12, no. 1 (2025): 1907–1917.

25. M. Dahmardeh and S. Aboli, "Lithium-Ion Battery SOC Estimation Using Adaptive Sliding Mode Observer and Wavelet Transform," *International Journal of Energy Research* 2025 (2025): 5582881.

26. Y. Qi, W. Zhao, X. Sun, L. Qi, D. Wang, and Y. Zhang, "State Estimation of Li-Ion Batteries via Improved Second-Order RC Model," *Energy Reports* 14 (2025): 31–42.

27. W. Lao-atiman, P. Bumroongsri, S. Olaru, and S. Kheawhom, "Real-Time State of Charge Estimation for Tri-Electrode Rechargeable Zinc–Air Flow Batteries via Pulse Response," *International Journal of Energy Research* 2025 (2025): 9928721.

28. K. Bhaskar, A. Kumar, J. Bunce, et al., "Heterogeneity-Induced Power and Capacity Loss in Parallel-Connected Cells," *IEEE Transactions on Transportation Electrification* 11, no. 2 (2024): 6305–6314.

ijer, 2026, 1, Downloaded from https://onlinelibrary.wiley.com/doi/10.1155/er/7965949 by Hanyang University Library, Wiley Online Library on [01/11/2026]. See the Terms and Conditions (https://onlinelibrary.wiley.com/terms-and-conditions) on Wiley Online Library for rules of use; OA articles are governed by the applicable Creative Commons License

29. L.-H. Lou, X.-T. Liang, J. Jiang, et al., "A Fused Electrical-Mechanical Model With Extended Kalman Filter and Adaptive Weighting for State-of-Charge Estimation of Lithium Iron-Phosphate Batteries," *eTransportation* 27 (2025): 100522.

30. R. P. Priya, S. R, and R. Sakile, "State of Charge Estimation of Lithium-Ion Battery Based on Extended Kalman Filter and Unscented Kalman Filter Techniques," *Energy Storage* 5, no. 3 (2023): e408.

31. F. Ahmed, K. Abulsaud, and A. M. Massoud, "On Equivalent Circuit Model-Based State-of-Charge Estimation for Lithium-Ion Batteries in Electric Vehicles," *IEEE Access* 13 (2025): 69950–69966.

32. D. N. T. How, M. A. Hannan, M. S. H. Lipu, et al., "SOC Estimation Using Deep Bidirectional Gated Recurrent Units With Tree Parzen Estimator Hyperparameter Optimization," *IEEE Transactions on Industry Applications* 58, no. 5 (2022): 6629–6638.

33. L. Liao, H. Li, W. Shang, and L. Ma, "An Empirical Study of the Impact of Hyperparameter Tuning and Model Optimization on the Performance Properties of Deep Neural Networks," *ACM Transactions on Software Engineering and Methodology (TOSEM)* 31, no. 3 (2022): 1–40.

34. J. Peng, J. Meng, J. Wu, et al., "A Comprehensive Overview and Comparison of Parameter Benchmark Methods for Lithium-Ion Battery Application," *Journal of Energy Storage* 71 (2023): 108197.

35. S. Nachimuthu, F. Alsaif, G. Devarajan, and I. Vairavasundaram, "Real Time SOC Estimation for Li-Ion Batteries in Electric Vehicles Using UKBF With Online Parameter Identification," *Scientific Reports* 15, no. 1 (2025): 1714.

36. J. Cao, S.-T. Quek, H. Xiong, and Z. Yang, "Comparison of Constrained Unscented and Cubature Kalman Filters for Nonlinear System Parameter Identification," *Journal of Engineering Mechanics* 149, no. 11 (2023): 04023088.

37. J.-H. Kim, E. Kwak, J. Jeong, and K.-Y. Oh, "Physics-Informed Markov Chain Model to Identify Degradation Pathways of Lithium-Ion Cells," *IEEE Transactions on Transportation Electrification* 10, no. 2 (2024): 3468–3481.

38. J. Oh, M. Lee, E. Ko, K. M. Kim, and J. Kim, "Comprehensive Understanding of the Effects of Imbalanced Cell via Battery Module Tests for Further Usage of Cycled Batteries," *Journal of Power Sources* 631 (2025): 236282.

39. S. Stock, J. Hagemeister, S. Grabmann, et al., "Cell Teardown and Characterization of an Automotive Prismatic LFP Battery," *Electrochimica Acta* 471 (2023): 143341.

40. H. Zhang, Y. Zhao, Y. Tian, Y. Zhang, Z. Tao, and S. Xu, "Multi-Level Optimization of Low-Temperature Heating Methods for Large-Capacity Lithium-Ion Batteries Based on Temperature Uniformity," *Energy* 330 (2025): 136628.

41. S. El Moutchou, H. Aziam, M. Mansori, and I. Saadoune, "Thermal Stability of Lithium-Ion Batteries: Case Study of NMC811 and LFP Cathode Materials," *Materials Today: Proceedings* 51 (2022): A1–A7.

42. J. Schmitt, I. Horstkötter, and B. Bäker, "State of Charge Estimation With Hysteresis-Prone Open Circuit Voltage in Lithium-Ion Batteries Using the Trajectory Correction Hysteresis (TCH) Model," *Journal of Power Sources Advances* 28 (2024): 100151.

43. E. Akbari and G. Z. Voyiadjis, "Stress and Strain Characterization for Evaluating Mechanical Safety of Lithium-Ion Pouch Batteries Under Static and Dynamic Loadings," *Batteries* 10, no. 9 (2024): 309.

44. D. Jeong and S. Bae, "Estimating Battery State-of-Charge With a Few Target Training Data by Meta-Learning," *Journal of Power Sources* 553 (2023): 232238.

45. J. Li, G. Bai, J. Yan, and J. Gu, "On-Line Parameter Identification and SOC Estimation of Nonlinear Model of Lithium-Ion Battery Based on Wiener Structure," *Journal of Energy Storage* 92 (2024): 112094.

46. L. Koltermann, M. C. Cortés, J. Figgener, S. Zurmühlen, and D. U. Sauer, "Improved Rule-Based Power Distribution Algorithm for Hybrid Battery Storage Systems and Real-World Validation," *Journal of Energy Storage* 86 (2024): 111360.

47. J. Dong, R. Wang, H. Wang, S. Hua, G. Geng, and Q. Jiang, "Adaptive SOC Estimation of Grid-Level BESS for Multiple Operational Scenarios," *Journal of Energy Storage* 132 (2025): 117776.

48. H. M. Hussein, A. Aghmadi, M. S. Abdelrahman, S. M. S. H. Rafin, and O. Mohammed, "A Review of Battery State of Charge Estimation and Management Systems: Models and Future Prospective," *WIREs Energy and Environment* 13, no. 1 (2024): e507.

49. Q. He, L. Fan, W. Huang, L. Zhao, and Z. Tan, "A Joint Model Identification and Battery SOC Estimation Method Based on ETASEKF," *IEEE Sensors Journal* 25, no. 16 (2025): 31807–31815.

50. X. He, K. Sun, Y. He, et al., "Mechanistic Insights Into the Dynamic Evolution Processes of LiFePO4/C Batteries," *Chemical Engineering Journal* 515 (2025): 163447.

51. T. Wu, C. Wang, Y. Hu, Z. Liang, and C. Fan, "Research on Electrochemical Characteristics and Heat Generating Properties of Power Battery Based on Multi-Time Scales," *Energy* 265 (2023): 126416.

52. R. Xiong, J. Huang, Y. Duan, and W. Shen, "Enhanced Lithium-Ion Battery Model Considering Critical Surface Charge Behavior," *Applied Energy* 314 (2022): 118915.

53. A. Umar, S. Mukhopadhyay, and A. Patra, "Improved State of Charge Estimation of a Li-Ion Cell Using a Fractional Order Model With Hysteresis," *Journal of Energy Storage* 103 (2024): 114114.

54. A. Van der Ven, K. A. See, and L. Pilon, "Hysteresis in Electrochemical Systems," *Battery Energy* 1, no. 2 (2022): 20210017.

55. D. Zhang, S. Park, L. D. Couto, V. Viswanathan, and S. J. Moura, "Beyond Battery State of Charge Estimation: Observer for Electrode-Level State and Cyclable Lithium With Electrolyte Dynamics," *IEEE Transactions on Transportation Electrification* 9, no. 4 (2022): 4846–4861.

56. Z. Zhou, Y. Ding, C. Li, et al., "Coupled Effect of Multiple Environmental Conditions on Thermal Runaway Behavior of NMC and LFP Lithium-Ion Batteries: Storage Environment Optimization Based on Cooling Efficiency and Space Utilization Rate: Coupled Effect of Multiple Environmental Conditions on Thermal Runaway," *Fire Technology* 61, no. 6 (2025): 3955–3978.

57. G. Zardalidis and F. Farmakis, "Study of the Correlation Between Electric and Mechanical/Thermal Parameters in a Graphite-LiFePO4 Pouch Cell," *Journal of Power Sources* 570 (2023): 233018.

58. Y. Li, K. Li, X. Liu, et al., "A Hybrid Machine Learning Framework for Joint SOC and SOH Estimation of Lithium-Ion Batteries Assisted With Fiber Sensor Measurements," *Applied Energy* 325 (2022): 119787.

59. M. Hossain, M. E. Haque, and M. T. Arif, "Online Model Parameter and State of Charge Estimation of Li-Ion Battery Using Unscented Kalman Filter Considering Effects of Temperatures and C-Rates," *IEEE Transactions on Energy Conversion* 37, no. 4 (2022): 2498–2511.

60. V. Selvaraj and I. Vairavasundaram, "A Bayesian Optimized Machine Learning Approach for Accurate State of Charge Estimation of Lithium Ion Batteries Used for Electric Vehicle Application," *Journal of Energy Storage* 86 (2024): 111321.

61. I. M. Monirul, L. Qiu, and R. Ruby, "Accurate State of Charge Estimation for UAV-Centric Lithium-Ion Batteries Using Customized Unscented Kalman Filter," *Journal of Energy Storage* 107 (2025): 114955.

62. L. Zhang, S. Yang, L. Liu, and P. Zhao, "Cell-to-Cell Variability in Li-Ion Battery Thermal Runaway: Experimental Testing, Statistical Analysis, and Kinetic Modeling," *Journal of Energy Storage* 56 (2022): 106024.

63. P. Li, J. Ye, J. Hou, Z. Deng, and S. Xiang, "State of Charge Estimation for Lithium-Ion Battery Using a Multi-Feature Mamba Network and UKF Under Mixed Operating Conditions," *Energy* 335 (2025): 137539.

ijer, 2026, 1, Downloaded from https://onlinelibrary.wiley.com/doi/10.1155/er/7965949 by Hanyang University Library, Wiley Online Library on [01/11/2026]. See the Terms and Conditions (https://onlinelibrary.wiley.com/terms-and-conditions) on Wiley Online Library for rules of use; OA articles are governed by the applicable Creative Commons License

64. L. Fuentes-Rodríguez, L. Abad, E. Pujades, P. Gómez-Romero, D. Tonti, and N. Casañ-Pastor, "Dramatic Drop in Cell Resistance Through Induced Dipoles and Bipolar Electrochemistry," *Journal of the Electrochemical Society* 169, no. 1 (2022): 016508.

65. T. Yang, Y. Li, P. Ren, et al., "Event-Triggered Robust State of Charge Estimation for Lithium-Ion Battery With Cloud-Integrated Battery Management System," *IEEE Transactions on Industrial Electronics* 73, no. 2 (2025): 2321–2332.

66. S. Buechele, E. Logan, T. Boulanger, et al., "Reversible Self-Discharge of LFP/Graphite and NMC811/Graphite Cells Originating From Redox Shuttle Generation," *Journal of the Electrochemical Society* 170, no. 1 (2023): 010518.

67. G. Wang, B. Jin, M. Wang, Y. Sun, Y. Zheng, and T. Su, "State of Charge Estimation for "LiFePO4-LiCoxNiyMn1-x-yO2" Hybrid Battery Pack," *Journal of Energy Storage* 65 (2023): 107345.

68. Z. Cui, J. Dai, J. Sun, D. Li, L. Wang, and K. Wang, "Hybrid Methods Using Neural Network and Kalman Filter for the State of Charge Estimation of Lithium-Ion Battery," *Mathematical Problems in Engineering* 2022 (2022): 9616124.

69. H. Obeid, R. Petrone, H. Chaoui, and H. Gualous, "Higher Order Sliding-Mode Observers for State-of-Charge and State-of-Health Estimation of Lithium-Ion Batteries," *IEEE Transactions on Vehicular Technology* 72, no. 4 (2023): 4482–4492.

70. R. Gayathri, M. F. Asma Ul Husna, R. Poojasri, S. Sutha, N. Pappa, and M. Vijayakarthick, "Hybrid Electro-Thermal Model Based Optimal Charging of Lithium-Ion Battery Using MOGA for Enhanced State-of-Health," *IFAC-PapersOnLine* 57 (2024): 173–178.

71. J. Peng, P. Takyi-Aninakwa, S. Wang, F. Masahudu, X. Yang, and J. M. Guerrero, "A Hybrid-Aided Approach With Adaptive State Update for Estimating the State-of-Charge of LiFePO4 Batteries Considering Temperature Uncertainties," *Journal of Energy Storage* 76 (2024): 109758.

72. R. Tang, J. Dong, C. Wang, et al., "A Comprehensive Review of the Research Progress on the Low-Temperature Performance of $LiFePO_4$ Batteries," *Carbon Neutralization* 4, no. 2 (2025): e70001.

73. R. Xu, S. Zhang, X. Shen, et al., "Unlocking the Polarization and Reversibility Limitations for Stable Low-Temperature Lithium Metal Anodes," *Small Structures* 4, no. 7 (2023): 2200400.

74. S.-T. Yun and S.-H. Kong, "Data-Driven In-Orbit Current and Voltage Prediction Using Bi-LSTM for LEO Satellite Lithium-Ion Battery SOC Estimation," *IEEE Transactions on Aerospace and Electronic Systems* 58, no. 6 (2022): 5292–5306.

75. H. Kauko, D. Pinel, I. Graabak, and O. Wolfgang, "Assessing the Potential of Seasonal Thermal Storage for Local Energy Systems: Case Study for a Neighborhood in Norway," *Smart Energy* 6 (2022): 100075.

76. G. Lian, M. Ye, Q. Wang, M. Wei, and Y. Ma, "Noise-Immune State of Charge Estimation for Lithium-Ion Batteries Based on Optimized Dynamic Model and Improved Adaptive Unscented Kalman Filter Under Wide Temperature Range," *Journal of Energy Storage* 64 (2023): 107223.

77. F. G. Erdinç, "Rolling Horizon Optimization Based Real-Time Energy Management of a Residential Neighborhood Considering PV and ESS Usage Fairness," *Applied Energy* 344 (2023): 121275.

78. Z. Liu, Y. Xiao, Y. Yuan, et al., "Fast Convergent on-Board Li-Ion Battery State of Charge Estimation via Back-Forth Moving Horizon Estimation," *IEEE Transactions on Power Electronics* 40, no. 9 (2025): 13187–13201.

79. Z. Zhang, H. Wang, L. Lu, et al., "State-of-Charge and Capacity Estimation for MWh-Scale LiFePO4 Peak-Shaving Battery Energy Storage Stations Based on Real-World Operating Data," *Energy* 339 (2025): 139086.

Appendix A. Pseudo-OCV Estimation Method.

The OCV at 50% SOC was determined by averaging the charge and discharge potentials. Subsequently, the OCV–SOC curve was refined by applying a linear interpolated approach: the charge-potential data were assigned higher weights to SOC values above 50%, where charging behavior was dominant. The discharge potential data were preferentially weighted to SOC values below 50%, where discharging behavior predominated. This procedure effectively mitigated hysteresis effects and yielded a representative pseudo–OCV curve. This relationship can be expressed as follows:

$$\begin{aligned}\mathrm{OCV}(\mathrm{SOC}) = {} & V_{\mathrm{charge}}(\mathrm{SOC}) \times \frac{100 - \mathrm{SOC}}{100} \\ & + V_{\mathrm{discharge}}(\mathrm{SOC}) \times \frac{\mathrm{SOC}}{100},\end{aligned} \tag{26}$$

where V_{charge} and $V_{\mathrm{discharge}}$ represent the charge and discharge potentials, respectively. This procedure was repeated for all datasets measured at different environmental temperatures and tabulated to embed the proposed method. Thus, the temperature dependence of the estimated OCV was calculated using the linear interpolation method from the lookup table in the model, which resulted in the OCV as the function of SOC and temperature.

Appendix B. Bayesian Optimization.

The parameters of the proposed method were selected to accurately approximate the underlying Gaussian distribution. The optimization aims to search for an optimized parameter x^* that yields the lowest loss function $f(x)$. The process for obtaining the lowest loss value of the loss function is as follows:

$$x^* = \underset{x \in X}{\operatorname{argmin}} f(x). \tag{27}$$

This function is defined as the objective function of the BO. This acquisition function was used to determine the criteria for selecting the following parameters as the estimated values of the objective function.

This study employs expected improvement (EI) as an acquisition function. The acquisition function EI is calculated as

$$\mathrm{EI}_{y^*}(x) = \int_{-\infty}^{y^*} (y^* - y) p(y|x) dy, \tag{28}$$

where y represents the value of the objective function according to parameter x. However, Equation (A2) shows a continuous feedback equation using large objective functions, resulting in a computational burden. Therefore, BO needs to be employed using a surrogate model for replacing the objective function, avoiding the computational burden of the continuous objective functions in Equation (A2) [62]. This study employed the Gaussian process (GP) as the general surrogate model because of its high convergence when optimizing multiple parameters for other surrogate models [62]. The GP-based surrogate model $p(y|x)$ was calculated using Bayes' rule as

$$p(y|x) = \frac{p(x|y) \times p(y)}{p(x)}. \tag{29}$$

The probability of the parameter values following the objective function $p(x|y)$ was calculated as

$$p(x|y) = \begin{cases} l(x) & \text{if } y < y^* \\ g(x) & \text{if } y \geq y^* \end{cases}, \tag{30}$$

ijer, 2026, 1, Downloaded from https://onlinelibrary.wiley.com/doi/10.1155/er/7965949 by Hanyang University Library, Wiley Online Library on [01/11/2026]. See the Terms and Conditions (https://onlinelibrary.wiley.com/terms-and-conditions) on Wiley Online Library for rules of use; OA articles are governed by the applicable Creative Commons License

where $l(x)$ and $g(x)$ represent the probability distributions of the comparison of the objective function values y and y^*. The newly defined EI equation using Equations (A2–A5) is expressed as

$$\mathrm{EI}_{y^*}(x) = \frac{\gamma y^* l(x) - l(x)\int_{-\infty}^{y^*} p(y)dy}{\gamma l(x) + (1-\gamma)g(x)} \propto \left(\gamma + \frac{g(x)}{l(x)}(1-\gamma)\right)^{-1}. \tag{31}$$

BO defines a parameter set that allows EI to have a minimum value using Equation (A6). The loop continues until the validation loss $f(x)$ converges to a minimum using Equation (A2).

ijer, 2026, 1, Downloaded from https://onlinelibrary.wiley.com/doi/10.1155/er/7965949 by Hanyang University Library, Wiley Online Library on [01/11/2026]. See the Terms and Conditions (https://onlinelibrary.wiley.com/terms-and-conditions) on Wiley Online Library for rules of use; OA articles are governed by the applicable Creative Commons License